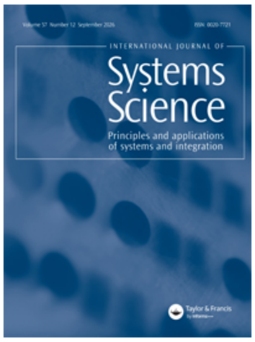

International Journal of Systems Science

ISSN: 0020-7721 (Print) 1464-5319 (Online) Journal homepage: www.tandfonline.com/journals/tsys20

Deep Bernoulli optimisation for solving 2D/3D ψ-tempered fractional optimal control problems

Parisa Rahimkhani & Thabet Abdeljawad

INTERNATIONAL JOURNAL OF SYSTEMS SCIENCE
https://doi.org/10.1080/00207721.2026.2622364

Deep Bernoulli optimisation for solving 2D/3D ψ-tempered fractional optimal control problems

Parisa Rahimkhani[a] and Thabet Abdeljawad[b,c,d]

[a]Faculty of Science, Mahallat Institute of Higher Education, Mahallat, Iran; [b]Department of Mathematics and Sciences, Prince Sultan University, Riyadh, Saudi Arabia; [c]Department of Fundamental Sciences, Faculty of Engineering and Architecture, Gelisim University, Avcilar-Istanbul, Turkiye; [d]Depertment of Medical Research, China Medical University, Taichung, Taiwan

ABSTRACT

This study introduces two- and three-dimensional optimal control problems characterised by the ψ-tempered fractional derivative and proposes a novel numerical methodology based on deep fractional-order Bernoulli optimisation to achieve their efficient solution. To this end, the problems under consideration are first reformulated as equivalent variational problems. Subsequently, a deep neural network employing the fractional-order Bernoulli functions and *sinh* as activation functions is utilised to approximate the state variable. To facilitate the effective implementation of the proposed method, we construct several integral operators of both integer and ψ-tempered fractional orders based on the basis functions derived from the deep neural network. These operators are discretised via the Fejér quadrature rule adapted to the ψ-tempered fractional calculus, ensuring stability and high-precision integration. The proposed approach converts the 2D/3D ψ-tempered fractional optimal control problem into an algebraic system using deep neural networks with integral operators and Gauss–Legendre integration, which is efficiently solved via Newton's method. The proposed method combines simple implementation, low computational cost, and high accuracy. Its effectiveness and robustness are validated through several representative 2D and 3D examples, confirming the method's applicability to complex fractional optimal control problems.

ARTICLE HISTORY
Received 8 October 2025
Accepted 9 January 2026

KEYWORDS
ψ-tempered fractional optimal control problems; deep neural network method; fractional-order Bernoulli functions; error estimate; collocation method

2020 MATHEMATICS SUBJECT CLASSIFICATIONS
26A33; 33F05; 92B20

1. Introduction

Fractional calculus provides a generalised mathematical framework in which differentiation and integration are extended to non-integer orders. While its origins date back nearly three centuries as a topic of pure mathematics, its significant role in science and engineering has only become prominent in recent decades. The distinctive feature of fractional derivatives is their inherent ability to incorporate memory and hereditary effects into mathematical models, enabling accurate descriptions of complex physical, biological, and socio-economic systems. Fractional differential equations (FDEs) have thus been successfully employed in diverse domains such as signal processing, electricity, electrochemistry, mechanic, and climate modelling (Carpinteri & Mainardi, 2014; Chakraborty & Veeresha, 2024). Depending on their kernel structure, fractional derivatives can be classified into singular types (e.g. Riemann-Liouville and Caputo) and non-singular types (e.g. Caputo-Fabrizio and Atangana-Baleanu), each offering unique modelling capabilities tailored to specific applications. The continuous development of analytical approaches and efficient numerical methods further reflects the increasing recognition of fractional calculus as a unifying bridge between mathematical theory and applied sciences. Among the most widely used approaches are homotopy perturbation (Zurigat et al., 2010), fractional-order Bernoulli functions (FBFs) (Rahimkhani et al., 2016), finite difference (Santra & Mohapatra, 2022), fractional chebyshev cardinal wavelet (Heydari et al., 2023), and physics informed neural network (Rahimkhani et al., 2025) method.

The ψ-Caputo fractional derivative generalises the classical Caputo operator by introducing a parameter-either a function or a constant-allowing the fractional order to adapt dynamically to the system's characteristics. This feature makes it particularly

CONTACT Thabet Abdeljawad tabdeljawad@psu.edu.sa Department of Mathematics and Sciences, Prince Sultan University, Riyadh, Saudi Arabia; Department of Fundamental Sciences, Faculty of Engineering and Architecture, Gelisim University, Avcilar-Istanbul, Turkiye; Depertment of Medical Research, China Medical University, Taichung, Taiwan

suitable for modelling phenomena with strong memory dependence and hereditary behaviour, as observed in viscoelasticity and anomalous diffusion. Unlike the standard Caputo derivative with a fixed power-law memory kernel, the ψ-Caputo form permits evolving memory kernels while retaining compatibility with initial value problems. The development of robust analytical and numerical methods is therefore essential, with approaches such as monotone iterative (Baitiche et al., 2021), finite difference (Li et al., 2024), ψ-fractional Genocchi wavelet (Rahimkhani & Abdeljawad, 2025), and extended Chebyshev cardinal wavelet (Heydari & Razzaghi, 2024) method widely employed to solve ψ-FDEs.

One type of fractional calculus of particular interest is the so-called tempered fractional calculus. Mathematically, it is of interest as the unique intersection between weighted fractional calculus and fractional calculus with analytic kernels. In modelling, it has been used to understand turbulence in geophysical flows (Meerschaert et al., 2014), and Levy processes such as Brownian motion (Baeumer & Meerschaert, 2010). Tempered fractional calculus is so important that it has been rediscovered at least twice under different names, as generalised proportional fractional calculus and as substantial fractional calculus (Mali et al., 2022). Li et al. (2015) examined various properties of tempered fractional derivatives and explored the existence, uniqueness, and stability of some tempered fractional ordinary differential equations. Zhao et al. (2016) demonstrated several properties involving function spaces and compositions, before considering variational calculus and spectral analysis for Riemann–Liouville-type tempered fractional differential equations. Morgado and Rebelo (2017) considered nonlinear Caputo-type tempered fractional differential equations with a terminal condition, analysed existence and uniqueness properties of the solution, and proposed three numerical techniques to approximate solutions of the considered problems. Zaky (2019) investigated the existence, uniqueness, and structural stability of solutions to nonlinear Caputo-type tempered fractional differential equations with generalised boundary conditions, and developed a spectral collocation technique for numerical solutions of the considered equations, including detailed convergence and error analysis.

Recently, the integration of ψ-fractional calculus (ψ-FC) and tempered fractional calculus (TFC) has emerged as a promising avenue for further research, enhancing the modelling capabilities for complex dynamical systems with memory and nonlocal properties. Fahad et al. (2021) proposed a comprehensive framework that unifies tempered and Hadamard-type fractional calculi by generalising the underlying operators with respect to an arbitrary monotonic function, known as ψ-TFC. This formulation can be considered a particular case of fractional calculus with analytic kernels (Oumarou et al., 2021) and weighted fractional calculus (Fernandez & Fahad, 2022). Moreover, Mali et al. (2022) rigorously analyzed ψ-tempered fractional differential equations, proving existence and uniqueness of solutions via the Banach fixed-point theorem and establishing their stability using Grönwall-type inequalities, thereby providing a solid theoretical foundation for the well-posedness of such models. Qiu et al. (2023) introduced two efficient numerical approaches for solving ψ-tempered integro-differential equations, thoroughly investigating the stability and convergence properties of the semi-discrete schemes, which ensures the robustness and reliability of these methods.

Control theory (Sayevand et al., 2022), rooted in the classical contributions of Pontryagin and colleagues, provides a framework for influencing the behaviour of dynamical systems toward desired objectives. Within this context, optimal control problems (OCPs) seek to minimise or maximise a performance index that depends on the system's dynamics. While traditional OCPs are already widely applied across disciplines such as economics, engineering, medicine, and biology, the extension of these problems to include fractional operators has given rise to the emerging field of fractional optimal control theory (FOCPs). FOCPs generalise classical OCPs by incorporating fractional derivatives in the system dynamics, the performance index, or both, thereby capturing memory and hereditary effects that classical models cannot represent. However, the nonlinear and nonlocal nature of fractional operators makes analytical solutions to FOCPs highly challenging, particularly in the presence of path constraints. Among these are techniques based on modified fractional homotopy (Qing & Pan, 2024), generalised Lerch polynomials (Javad Ebadi, 2025), and orthonormal piecewise Chelyshkov functions (Heydari & Razzaghi, 2022) method, which primarily solves unconstrained problems. For constrained FOCPs, where analytical treatment is almost infeasible, attention has shifted toward powerful numerical strategies, including Chebyshev wavelet (Xu et al., 2021), generalised fractional Chebyshev functions (Rabiei & Parand, 2020), and Müntz-Legendre polynomials (Rahimkhani et al., 2023) method. Collectively, these advances highlight the central importance of numerical approaches in solving FOCPs and underscore their growing role in bridging theory with real-world applications.

The lack of sufficient research on two- and three-dimensional FOCPs, combined with the advantageous features of the ψ-tempered fractional derivative (ψ-TFD), has motivated our study to solve these problems in 2D and 3D settings. The resulting formulations are given as follows:

(a) *2D-ψ-TFOCPs:*

$$\min \mathcal{J}[\mathcal{U},\mathcal{V}] = \int_0^1 \int_0^1 \mathcal{G}(x,t,\mathcal{U}(x,t),\mathcal{V}(x,t))\,\mathrm{d}x\,\mathrm{d}t, \quad (1)$$

under the following constraint:

$$\begin{cases} {}^{TC}\mathcal{D}^{\zeta,\lambda}_{\psi,t}\mathcal{U}(x,t) = a_1\mathcal{U}_{xx}(x,t) + a_2\mathcal{U}_x(x,t) \\ \quad +\mathcal{V}(x,t) + \mathcal{F}(x,t,\mathcal{U}), \\ \mathcal{U}(x,0) = f(x), \quad 0 < x \le 1, \\ \mathcal{U}(0,t) = g_1(t), \quad \mathcal{U}(1,t) = g_2(t), \\ \quad 0 < t \le 1. \end{cases} \quad (2)$$

(b) *3D-ψ-TFOCPs:*

$$\min \mathcal{J}[\mathcal{U},\mathcal{V}] = \int_0^1 \int_0^1 \int_0^1 \mathcal{G}(x,y,t,\mathcal{U}(x,y,t), \mathcal{V}(x,y,t))\,\mathrm{d}x\,\mathrm{d}y\,\mathrm{d}t, \quad (3)$$

under the following constraint:

$$\begin{cases} {}^{TC}\mathcal{D}^{\zeta,\lambda}_{\psi,t}\mathcal{U}(x,y,t) = a_1\mathcal{U}_{xx}(x,y,t) \\ \quad + a_2\mathcal{U}_{yy}(x,y,t) + a_3\mathcal{U}_x(x,y,t) \\ \quad +\mathcal{V}(x,y,t) + \mathcal{F}(x,y,t,\mathcal{U}), \\ \mathcal{U}(x,y,0) = f(x,y), \quad 0 < x,y \le 1, \\ \mathcal{U}(x,0,t) = h_1(x,t), \quad \mathcal{U}(x,1,t) = h_2(x,t), \\ \quad 0 < x,t \le 1, \\ \mathcal{U}(0,y,t) = g_1(y,t), \quad \mathcal{U}(1,y,t) = g_2(y,t), \\ \quad 0 < y,t \le 1. \end{cases} \quad (4)$$

Here, $\mathcal{U}$ and $\mathcal{V}$ denote the state and control variables, respectively. The functions $\mathcal{G},\mathcal{F},f,h_1,h_2,g_1$ and g_2 are assumed to be known and continuous over their respective domains of definition, and $a_i, i = 1,2,3$ are given number. Also, ${}^{TC}\mathcal{D}^{\zeta,\lambda}_{\psi,t}$ is the ψ-tempered fractional derivative of Caputo type of order ζ with tempering index $\lambda \in \mathbb{R}$.

Since the advent of deep neural networks (DNNs) (Hinton et al., 2006), deep learning has gained remarkable attention and widespread use. These approaches have been successfully utilised in diverse domains such as speech recognition (Nassif et al., 2019), complex spatio-temporal dynamic systems (Vaziri & Fang, 2025), and image analysis (Yang et al., 2018). Although most implementations rely on DNNs primarily as regression frameworks, growing research efforts have begun to explore their potential in solving of differential equations. Hajimohammadi et al. (2021) employed a Legendre-based DNNs for solving nonlinear Volterra-Fredholm-Hammerstein integral equations. Dufera (2021) employed DNNs to solve systems of differential equations, proposing a vectorised algorithm implemented in Python. Guo et al. (2021) proposed a deep collocation method for thin plate bending problems. Rahimkhani (2023) applied the fractional-order Genocchi DNN to solve a class of nonlinear stochastic differential equations influenced by fractional Brownian motion.

In this work, the considered problems are initially recast into a variational formulations. A DNN equipped with a fractional-order Bernoulli activation function is then adopted to approximate the associated state variable. To enable practical realisation of the proposed framework, a family of integral operators of both integer and ψ-tempered fractional type are defined, constructed directly from the network's basis functions. By combining these operators with the structural properties of the DNN, the 2D and 3D-ψ-TFOCPs are reformulated as finite-dimensional algebraic systems. The discretisation relies on 2D/3D Gauss–Legendre integration rules, leading to a nonlinear algebraic model that can be efficiently handled through Newton's iterative procedure. The main contributions and innovative aspects of the proposed framework can be summarised as follows:

- *Generalized ψ-tempered fractional formulation:* This work introduces a fully generalised 2D/3D ψ-tempered fractional optimal control framework that (Li et al., 2015; Mali et al., 2022), unlike classical approaches, (1) captures nonlocal and memory-dependent dynamics, (2) incorporates a flexible ψ-function to accurately model a wide range of complex system behaviours, (3) employs tempering to ensure physically realistic and bounded memory effects, (4) enhances numerical stability and convergence, and (5) enables smooth transition between fractional and classical behaviours, providing robust applicability for real-world engineering and physical problems.
- *Deep fractional-order Bernoulli approximation:* A novel deep neural network architecture equipped with fractional-order Bernoulli functions and the *sinh* activation function is developed. The proposed framework leverages deep neural networks to efficiently approximate solutions of high-dimensional and nonlinear ψ-tempered fractional optimal control problems. The DNNs provide continuous and differentiable solutions, allow evaluation at arbitrary points, and offer high accuracy even with a relatively small number of parameters. Their powerful function approximation capability enables modelling complex multivariable interactions, while their flexibility and generalisation ensure robust performance across diverse system dynamics, surpassing classical numerical methods in both efficiency and scalability.
- *Direct construction of ψ-tempered integral operators:* The ψ-tempered fractional and integer-order integral operators are constructed directly from the DNN basis functions without introducing auxiliary approximations. Such direct operator construction is uncommon in conventional numerical techniques and leads to improved stability, accuracy, and consistency of the discretised scheme.
- *High-order discretization via Fejér and Gauss–Legendre quadrature:* The incorporation of Fejér quadrature (adapted to ψ-tempered operators) and 2D/3D Gauss–Legendre rules results in highly accurate integral evaluation, ensuring robust and stable discretization even in complex multidimensional domains.
- *Efficient algebraic reformulation and fast solvers:* The overall framework reduces the 2D/3D ψ-TFOCPs to a finite-dimensional nonlinear algebraic system that can be efficiently solved using Newton's iterative procedure, thereby achieving low computational cost and fast convergence.

The structure of the current research is presented as follows: In Section 2, we review the definitions of the ψ-tempered fractional integral (ψ-TFI) and derivative operators along with their main properties, and also provide an overview of DNNs. Section 3 starts by presenting the fundamental integral operators and then details the proposed numerical scheme for solving 3D-ψ-TFOCPs. Section 4 focuses on establishing the error estimate for the approximated cost function. Section 5 illustrates the proposed approach through three numerical examples and their respective simulation outcomes, highlighting its effectiveness. Concluding remarks are given in Section 6.

2. Preliminary framework

This section presents a detailed overview of the fundamental definitions of ψ-tempered fractional calculus within the domain $\Upsilon = [0,1] \times [0,1] \times [0,1]$. In addition, the fractional-order Bernoulli deep neural network (FBDNN) framework, and some of their properties are introduced.

2.1. ψ-tempered fractional calculus

Definition 2.1 (Mali et al., 2022): Let $\mathcal{U}$ denote an absolutely ψ-integrable function defined on the domain Υ, where $\psi \in C^1([0,1])$ is a strictly increasing function satisfying $\psi'(t) \neq 0$ for all $t \in [0,1]$. Then, the ψ-TFI of $\mathcal{U}$, of order $\zeta > 0$ with tempering index $\lambda \in \mathbb{R}$, is defined as follows:

$$
{}^{T}\mathcal{I}^{\zeta,\lambda}_{\psi,t}\mathcal{U}(x,y,t) = \frac{1}{\Gamma(\zeta)} \int_0^t \psi'(\varsigma)(\psi(t)-\psi(\varsigma))^{\zeta-1} \times e^{-\lambda(\psi(t)-\psi(\varsigma))}\mathcal{U}(x,y,\varsigma)\,\mathrm{d}\varsigma. \quad (5)
$$

Definition 2.2 (Mali et al., 2022): Let $\mathcal{U}$ belong to the space $AC^n_{\psi,t}(\Upsilon)$ as defined in Mali et al. (2022), and let $\psi \in C^n([0,1])$ be a strictly increasing function satisfying $\psi'(t) \neq 0$ for all $t \in [0,1]$. Then, the ψ-TFD of Caputo type for the function $\mathcal{U}$, of order $\zeta \in (n-1,n)$ with tempering index $\lambda \in \mathbb{R}$, is defined as follows:

$$
{}^{TC}\mathcal{D}^{\zeta,\lambda}_{\psi,t}\mathcal{U}(x,y,t) = {}^{T}\mathcal{I}^{n-\zeta,\lambda}_{\psi,t}\left(\frac{1}{\psi'(t)}.\frac{\mathrm{d}}{\mathrm{d}t}+\lambda\right)^n \mathcal{U}(x,y,t). \quad (6)
$$

Proposition 2.1 (Mali et al., 2022): *Assume that $\zeta \in (0,\infty)$, $\lambda \in \mathbb{R}$, and $\beta \in (-1,\infty)$. Under these assumptions, the following results are established:*

$$
\begin{aligned}
&{}^{T}\mathcal{I}^{\zeta,\lambda}_{\psi,t}(e^{-\lambda\psi(t)}(\psi(t)-\psi(0))^{\beta}) \\
&\quad = \frac{\Gamma(\beta+1)}{\Gamma(\beta+\zeta+1)} e^{-\lambda\psi(t)}(\psi(t)-\psi(0))^{\beta+\zeta}, \\
&{}^{T}\mathcal{I}^{\zeta,\lambda}_{\psi,t}((\psi(t)-\psi(0))^{\beta}) \\
&\quad = \frac{\Gamma(\beta+1)}{\Gamma(\beta+\zeta+1)} e^{-\lambda(\psi(t)-\psi(0))}(\psi(t)-\psi(0))^{\beta+\zeta} \\
&\qquad \times {}_1F_1(\beta+1;\beta+\zeta+1;\lambda(\psi(t)-\psi(0))), \quad (7) \\
&{}^{T}\mathcal{I}^{\zeta,\lambda}_{\psi,t}(1) = e^{-\lambda(\psi(t)-\psi(0))}(\psi(t)-\psi(0))^{\zeta} \\
&\qquad \times E_{1,1+\zeta}(\lambda(\psi(t)-\psi(0))),
\end{aligned}
$$

for $\beta > \lfloor \zeta \rfloor$

$$
\begin{aligned}
&{}^{TC}\mathcal{D}^{\zeta,\lambda}_{\psi,t}(e^{-\lambda\psi(t)}(\psi(t)-\psi(0))^{\beta}) \\
&\quad = \frac{\Gamma(\beta+1)}{\Gamma(\beta-\zeta+1)} e^{-\lambda\psi(t)}(\psi(t)-\psi(0))^{\beta-\zeta}, \\
&{}^{TC}\mathcal{D}^{\zeta,\lambda}_{\psi,t}((\psi(t)-\psi(0))^{\beta}) \\
&\quad = \frac{\Gamma(\beta+1)}{\Gamma(\beta-\zeta+1)} e^{-\lambda(\psi(t)-\psi(0))}(\psi(t)-\psi(0))^{\beta-\zeta} \\
&\qquad \times {}_1F_1(\beta+1;\beta-\zeta+1;\lambda(\psi(t)-\psi(0))), \quad (8) \\
&{}^{TC}\mathcal{D}^{\zeta,\lambda}_{\psi,t}(1) = \lambda^{n} e^{-\lambda(\psi(t)-\psi(0))}(\psi(t)-\psi(0))^{n-\zeta} \\
&\qquad \times E_{1,n+1-\zeta}(\lambda(\psi(t)-\psi(0))),
\end{aligned}
$$

where ${}_1F_1(a;c;z)$ is the well-known Kummer's function or confluent hypergeometric function, $n-1<\zeta<n$, and $E_{a,b}$ is the two-parameter Mittag-Leffler function.

Theorem 2.1 (Mali et al., 2022): *Let $\zeta \in (0,\infty)$, and $\lambda \in \mathbb{R}$, then we have*

(i) *If $n-1<\zeta<n \in \mathbb{N}$ and $\mathcal{U} \in C^{n}_{t}(\Upsilon)$, then ${}^{TC}\mathcal{D}^{\zeta,\lambda}_{\psi,t}\,{}^{T}\mathcal{I}^{\zeta,\lambda}_{\psi,t}\mathcal{U}(x,y,t) = \mathcal{U}(x,y,t)$,*
(ii) *If $n-1<\zeta<n \in \mathbb{N}$ and $\mathcal{U} \in AC^{n}_{\psi,t}(\Upsilon)$, then*

$$
\begin{aligned}
&{}^{T}\mathcal{I}^{\zeta,\lambda}_{\psi,t}\,{}^{TC}\mathcal{D}^{\zeta,\lambda}_{\psi,t}\mathcal{U}(x,y,t) \\
&\quad = \mathcal{U}(x,y,t) - e^{-\lambda\psi(t)} \sum_{j=0}^{n-1} \frac{(\psi(t)-\psi(0))^{j}}{j!} \\
&\qquad \times \left(\left(\frac{1}{\psi'(t)} \cdot \frac{\mathrm{d}}{\mathrm{d}t} \right)^{j} (e^{\lambda\psi(t)}\mathcal{U}(x,y,t)) \right)\Big|_{t=0}.
\end{aligned}
$$

Theorem 2.2 (Mali et al., 2022): *If $\zeta_1,\zeta_2 \in (0,\infty)$ and $\lambda \in \mathbb{R}$, such that $\lfloor \zeta_2 \rfloor < \lfloor \zeta_1 \rfloor$, then*

$$
{}^{TC}\mathcal{D}^{\zeta_2,\lambda}_{\psi,t}\,{}^{T}I^{\zeta_1,\lambda}_{\psi,t}\mathcal{U}(x,y,t) = {}^{T}I^{\zeta_1-\zeta_2,\lambda}_{\psi,t}\mathcal{U}(x,y,t).
$$

2.2. Deep neural network

The primary motivation behind the introduction of the FBDNN is its application to the solution of complex differential models. This framework extends the role of deep learning in scientific computing, with a particular emphasis on the accurate and efficient solution of differential equations. The FBDNN integrates the strengths of deep learning architectures with those of numerical methods, such as the collocation technique, thereby providing a hybrid computational tool that enhances the accuracy and robustness of the obtained solutions.

Conceptually, the FBDNN is structured as a combination of two interconnected subnetworks. The first subnetwork is a feed-forward neural network augmented with a layer of FBFs, designed to approximate the solution of the underlying model. The second subnetwork consists of a sequence of operation nodes, which incorporate essential mathematical operators such as differentiation, integration, and numerical quadrature, to ensure that the approximate solution satisfies the governing differential system. Specifically, the integral operators of both integer and ψ-tempered fractional orders, the Legendre-Gauss quadrature and Fejér quadrature formula are embedded into this architecture to accelerate convergence and improve solution accuracy.

The architecture of the first subnetwork, consisting of $\mathcal{N}$- layers, can be expressed as follows Rahimkhani (2023):

$$
\begin{cases}
\mathbf{D}_0 = x, \quad x \in R^{\varrho}, \\
\mathbf{D}_1 = B^{\epsilon}(\mathbf{W}^{(1)}\mathbf{D}_0 + b^{(1)}), \\
\mathbf{D}_i = f(\mathbf{W}^{(i)}\mathbf{D}_{i-1} + b^{(i)}), \quad 2 \le i \le \mathcal{N}-1, \\
\mathbf{D}_{\mathcal{N}} = \mathbf{W}^{(\mathcal{N})}\mathbf{D}_{\mathcal{N}-1} + b^{(\mathcal{N})}.
\end{cases} \tag{9}
$$

Here $\mathbf{D}_0$ represents the input layer, $\mathbf{D}_i, 1 \le i \le \mathcal{N}-1$ denote the hidden layers, and $\mathbf{D}_{\mathcal{N}}$ is the output layer. The activation function is denoted by f, while $\mathbf{W}^{(i)}$ and $b^{(i)}$ represent, respectively, the weight vectors and bias parameters associated with the ith layer. The expression $B^{\epsilon}(x) = [B^{\epsilon}_0(x), B^{\epsilon}_1(x), \ldots, B^{\epsilon}_{\hat{m}}(x)]^{T}$, denotes the vector of FBFs, where each $B^{\epsilon}_i(x), i = 0, 2, \ldots, \hat{m}$, represents an individual FBFs, defined over the interval

$[0,1]$ as follows Rahimkhani et al. (2016):

$$B_i^{\epsilon}(t) = \sum_{r=0}^{i} \binom{i}{r} \mathcal{B}_{i-r} x^{r\epsilon}, \quad i = 0, 1, \ldots, m, \quad (10)$$

where $\mathcal{B}_i, i = 0, 1, \ldots, m$ are the Bernoulli numbers.

Any continuous function $\mathcal{U}(x,t)$ belonging to the space $L^2([0,1] \times [0,1])$ can be approximate as

$$\mathcal{U}(x,t) \simeq \mathbf{D}_{\mathcal{N}}(x,t,\tilde{U}), \quad (11)$$

where

$$\tilde{U} = [\tilde{u}_{i,j}]_{(m+1)\times(\tilde{m}+1)}.$$

Furthermore, for any continuous function $\mathcal{U}(x,y,t)$ belonging to the Hilbert space $L^2([0,1] \times [0,1] \times [0,1])$, the following approximation can be employed:

$$\mathcal{U}(x,y,t) \simeq \mathbf{D}_{\mathcal{N}}(x,y,t,U), \quad (12)$$

where

$$U = [u_{i,k}]_{(m+1)^2\times(\tilde{m}+1)}.$$

The second network is designed to solve the proposed models under consideration. To achieve this, it employs operation nodes corresponding to derivatives, integrals, and related operators. Moreover, Legendre–Gaussian quadrature and standard differentiation techniques are incorporated within the network to enhance both accuracy and computational efficiency. The training process is carried out such that the prescribed cost function is minimised.

Remark 2.1: The selection of training data plays a critical role in the efficiency of the FBDNN. To construct an adaptive scheme, collocation points should be concentrated in regions where the solution exhibits rapid variations or high-frequency behaviour. Various strategies are available for choosing these points, including equidistant discretization or roots of orthogonal polynomials. In this study, the roots of Nth-order Legendre polynomials were employed to generate the training dataset.

Remark 2.2: Justification of the choice of fractional-order Bernoulli polynomials as basis functions: according to Mashayekhi et al. (2013), the Bernoulli polynomials form a complete basis over the interval $[0,1]$. For approximating an arbitrary time function, the advantages of Bernoulli polynomials $B_i(t), i = 0, 1, \ldots$ over the shifted Legendre polynomials $P_i(t)$, $i = 0, 1, \ldots$ are:

- The Bernoulli polynomials have less terms than the shifted Legendre polynomials. For example, $B_6(t)$ has 5 terms, while $P_6(t)$ has 7 terms, and this difference will increase by increasing i. Hence, for approximating an arbitrary function, we use less CPU time by applying the Bernoulli polynomials as compared to the shifted Legendre polynomials.
- The coefficient of individual terms in the Bernoulli polynomials $B_i(t)$, are smaller than the coefficient of individual terms in the shifted Legendre polynomials $P_i(t)$. Since the computational errors in the product are related to the coefficients of individual terms, the computational errors are less by using the Bernoulli polynomials.

3. Formulation of deep Bernoulli optimisation method

In this section, we present a novel numerical framework that integrates the FBFs collocation method with DNNs for the efficient solution of 3D-ψ-TFOCPs. To establish the foundation of the proposed approach, we first derive the essential integer-order and ψ-TFI operators, which constitute the core building blocks of the computational methodology.

3.1. Required integral operators

The ψ-TFI operator of order $\zeta > 0$ with tempering parameter $\lambda \in \mathbb{R}$, corresponding to the function $\mathbf{D}_{\mathcal{N}}(x,y,t,U)$, is formally defined as follows:

$$\Phi_1(x,y,t,\zeta) = {}^{T}\mathcal{I}_{\psi,t}^{\zeta,\lambda} \mathbf{D}_{\mathcal{N}}(x,y,t,U). \quad (13)$$

UtilisingUtilizing the definition of the ψ-TFI in combination with the Fejér quadrature rule (Youssri & Atta, 2024), we derive the following expression:

$$\begin{aligned}
&\Phi_1(x,y,t,\zeta) \\
&= \frac{1}{\Gamma(\zeta)} \int_0^t \psi'(\vartheta)(\psi(t) - \psi(\vartheta))^{\zeta-1} \\
&\quad \times e^{-\lambda(\psi(t)-\psi(\vartheta))} \mathbf{D}_{\mathcal{N}}(x,y,\vartheta,U)\, d\vartheta \\
&= \frac{t}{\Gamma(\zeta)} \sum_{k=0}^{n^*} \omega_k \psi'\left(t\left(\frac{1+\nu_k}{2}\right)\right)
\end{aligned}$$

$$\times\left(\psi(t)-\psi\left(t\left(\frac{1+\nu_k}{2}\right)\right)\right)^{\zeta-1}$$
$$\times e^{-\lambda\left(\psi(t)-\psi\left(t\left(\frac{1+\nu_k}{2}\right)\right)\right)}$$
$$\times \mathbf{D}_{\mathcal{N}}\left(x,y,t\left(\frac{1+\nu_k}{2}\right),U\right), \tag{14}$$

where

$$\nu_k=\cos(v_k),\quad \omega_k=\frac{2\sin(v_k)}{n^*}\sum_{i=0}^{\lfloor\frac{n^*}{2}\rfloor}\frac{\sin((2i-1)v_i)}{2i-1},$$

and

$$v_k=\frac{k\pi}{n^*},\quad k=0,1,\ldots,n^*.$$

The second-order integral of the function $\Phi_1(x,y,t,\zeta)$ with respect to the variables x and y is expressed as follows:

$$\begin{aligned}\Phi_2(x,y,t,\zeta)&=\mathcal{I}_x^2\Phi_1(x,y,t,\zeta),\\ \Phi_3(x,y,t,\zeta)&=\mathcal{I}_y^2\Phi_1(x,y,t,\zeta).\end{aligned} \tag{15}$$

Applying the Fejér quadrature formula, we obtain the following results:

$$\begin{aligned}&\Phi_2(x,y,t,\zeta)\\ &=\int_0^x(x-\vartheta)\Phi_1(\vartheta,y,t,\zeta)\,\mathrm{d}\vartheta\\ &=x\sum_{k=0}^{n^*}\omega_k\left(x-x\left(\frac{1+\nu_k}{2}\right)\right)\\ &\quad\times\Phi_1\left(x\left(\frac{1+\nu_k}{2}\right),y,t,\zeta\right),\end{aligned} \tag{16}$$

and

$$\begin{aligned}&\Phi_3(x,y,t,\zeta)\\ &=\int_0^y(y-\vartheta)\Phi_1(x,\vartheta,t,\zeta)\,\mathrm{d}\vartheta\\ &=y\sum_{k=0}^{n^*}\omega_k\left(y-y\left(\frac{1+\nu_k}{2}\right)\right)\\ &\quad\times\Phi_1\left(x,y\left(\frac{1+\nu_k}{2}\right),t,\zeta\right).\end{aligned} \tag{17}$$

By Utilizing the previously outlined methods, the remaining required integrals can similarly be computed

$$\begin{aligned}\Phi_4(x,y,t,\zeta)&=\mathcal{I}_x^2\Phi_3(x,y,t,\zeta),\\ \Phi_5(x,y,t)&=\mathcal{I}_x^2\mathbf{D}_{\mathcal{N}}(x,y,t,U),\\ \Phi_6(x,y,t)&=\mathcal{I}_y^2\Phi_5(x,y,t),\\ \Phi_7(x,y,t,\zeta)&=\mathcal{I}_x\Phi_4(x,y,t,\zeta).\end{aligned} \tag{18}$$

Remark 3.1: The Fejér quadrature formula (Youssri & Atta, 2024) has garnered widespread recognition and adoption due to its remarkable efficiency, accuracy, and the inherent simplicity that characterises its implementation. One of its key advantages lies in the ease with which error estimates can be derived, providing practitioners with valuable insights into the reliability of the obtained results. When adapted to ψ-tempered fractional calculus, this quadrature formula offers several additional benefits. It enables highly accurate numerical integration by efficiently capturing the behaviour of ψ-tempered fractional operators over the entire integration interval. Its spectral nature allows smooth handling of weak singularities and nonlocal memory effects inherent in fractional operators, while maintaining computational efficiency. Moreover, when combined with deep Bernoulli neural network approximations, Fejér quadrature ensures stable and accurate evaluation of ψ-tempered fractional integrals, making it particularly suitable for complex multidimensional applications.

3.2. Procedure

To solve problem (3)-(4), the term $\frac{\partial^{\zeta+4}}{\partial t^{\zeta}\partial x^2\partial y^2}\mathcal{U}(x,y,t)$ is approximated using the FBDNN framework as follows:

$$\frac{\partial^{\zeta+4}}{\partial t^{\zeta}\partial x^2\partial y^2}\mathcal{U}(x,y,t)=\mathbf{D}_{\mathcal{N}}(x,y,t,U), \tag{19}$$

where ${}^{TC}\mathcal{D}_{\psi}^{\zeta,\lambda}=\frac{\partial^{\zeta}}{\partial t^{\zeta}}$.

Applying the operator ${}^{T}\mathcal{I}_{\psi,t}^{\zeta,\lambda}$ to both side of Equation (19), we obtain the following formulation:

$$\frac{\partial^4}{\partial x^2\partial y^2}\mathcal{U}(x,y,t)=\Phi_1(x,y,t,\zeta)+e^{-\lambda(\psi(t)-\psi(0))}\times\frac{\partial^4}{\partial x^2\partial y^2}f(x,y). \tag{20}$$

When the operator $\mathcal{I}_x^2$ is applied to both side of Equation (20), the resulting expression is obtained as:

$$\frac{\partial^2}{\partial y^2}\mathcal{U}(x,y,t) = \Phi_2(x,y,t,\zeta) + e^{-\lambda(\psi(t)-\psi(0))} \left(\frac{\partial^2}{\partial y^2}f(x,y) - \frac{\partial^2}{\partial y^2}f(x,y)\Big|_{x=0} - x\frac{\partial}{\partial x}\left(\frac{\partial^2}{\partial y^2}f(x,y)\right)\Big|_{x=0}\right) + \frac{\partial^2}{\partial y^2}\mathcal{U}(x,y,t)\Big|_{x=0} + x\frac{\partial}{\partial x}\left(\frac{\partial^2}{\partial y^2}\mathcal{U}(x,y,t)\right)\Big|_{x=0}. \quad (21)$$

By substituting $x = 1$ into Equation (21), the corresponding expression for $\frac{\partial}{\partial x}(\frac{\partial^2}{\partial y^2}\mathcal{U}(x,y,t))|_{x=0}$ is derived as follows:

$$\frac{\partial}{\partial x}\left(\frac{\partial^2}{\partial y^2}\mathcal{U}(x,y,t)\right)\Big|_{x=0} = \frac{\partial^2}{\partial y^2}g_2(y,t) - \Phi_2(1,y,t,\zeta) - e^{-\lambda(\psi(t)-\psi(0))} \times \left(\frac{\partial^2}{\partial y^2}f(1,y) - \frac{\partial^2}{\partial y^2}f(0,y) - \left(\frac{\partial^3}{\partial x\partial y^2}f(x,y)\right)\Big|_{x=0}\right) - \frac{\partial^2}{\partial y^2}g_1(y,t). \quad (22)$$

From Equations (21) and (22), it follows that:

$$\frac{\partial^2}{\partial y^2}\mathcal{U}(x,y,t) = \Phi_2(x,y,t,\zeta) + e^{-\lambda(\psi(t)-\psi(0))} \times \left(\frac{\partial^2}{\partial y^2}f(x,y) - \frac{\partial^2}{\partial y^2}f(0,y) - x\left(\frac{\partial^3}{\partial x\partial y^2}f(x,y)\right)\Big|_{x=0}\right) + \frac{\partial^2}{\partial y^2}g_1(y,t) + x\Bigg[\frac{\partial^2}{\partial y^2}g_2(y,t) - \Phi_2(1,y,t,\zeta) - e^{-\lambda(\psi(t)-\psi(0))} \times \left(\frac{\partial^2}{\partial y^2}f(1,y) - \frac{\partial^2}{\partial y^2}f(0,y) - \left(\frac{\partial^3}{\partial x\partial y^2}f(x,y)\right)\Big|_{x=0}\right) - \frac{\partial^2}{\partial y^2}g_1(y,t)\Bigg] = \mathcal{U}^*_{yy}(x,y,t). \quad (23)$$

Applying the integer-order integral operator $\mathcal{I}_y^2$ to both sides of Equation (20), we obtain:

$$\frac{\partial^2}{\partial x^2}\mathcal{U}(x,y,t) = \Phi_3(x,y,t,\zeta) + e^{-\lambda(\psi(t)-\psi(0))} \times \left(\frac{\partial^2}{\partial x^2}f(x,y) - \frac{\partial^2}{\partial x^2}f(x,y)\Big|_{y=0} - y\frac{\partial}{\partial y}\left(\frac{\partial^2}{\partial x^2}f(x,y)\right)\Big|_{y=0}\right) + \frac{\partial^2}{\partial x^2}\mathcal{U}(x,y,t)\Big|_{y=0} + y\frac{\partial}{\partial y}\left(\frac{\partial^2}{\partial x^2}\mathcal{U}(x,y,t)\right)\Big|_{y=0}. \quad (24)$$

Substituting $y = 1$ into Equation (24), we achieve the corresponding expression for $\frac{\partial}{\partial y}(\frac{\partial^2}{\partial x^2}\mathcal{U}(x,y,t))|_{y=0}$ as follows:

$$\frac{\partial}{\partial y}\left(\frac{\partial^2}{\partial x^2}\mathcal{U}(x,y,t)\right)\Big|_{y=0} = \frac{\partial^2}{\partial x^2}h_2(x,t) - \Phi_3(x,1,t,\zeta) - e^{-\lambda(\psi(t)-\psi(0))}\left(\frac{\partial^2}{\partial x^2}f(x,1) - \frac{\partial^2}{\partial x^2}f(x,0) - \left(\frac{\partial^3}{\partial y\partial y^2}f(x,y)\right)\Big|_{y=0}\right) - \frac{\partial^2}{\partial x^2}h_1(x,t). \quad (25)$$

From the conjunction of Equations (24) and (25), the following result is obtained:

$$\frac{\partial^2}{\partial x^2}\mathcal{U}(x,y,t) = \Phi_3(x,y,t,\zeta) + e^{-\lambda(\psi(t)-\psi(0))} \times \left(\frac{\partial^2}{\partial x^2}f(x,y) - \frac{\partial^2}{\partial x^2}f(x,0) - y\left(\frac{\partial^3}{\partial y\partial x^2}f(x,y))\Big|_{y=0}\right) + \frac{\partial^2}{\partial x^2}h_1(x,t) + y\Bigg[\frac{\partial^2}{\partial x^2}h_2(x,t)$$

$$
\begin{aligned}
&- \Phi_3(x,1,t,\zeta) - e^{-\lambda(\psi(t)-\psi(0))} \\
&\times \left(\frac{\partial^2}{\partial x^2}f(x,1) - \frac{\partial^2}{\partial x^2}f(x,0) \right.\\
&\left. - \left(\frac{\partial^3}{\partial y \partial x^2}f(x,y)\right)\Bigg|_{y=0}\right) \\
&\left. - \frac{\partial^2}{\partial x^2}h_1(x,t)\right] = \mathcal{U}^*_{xx}(x,y,t).
\end{aligned} \tag{26}
$$

Employing the operator $\mathcal{I}_x^2$ to both sides of Equation (26), we yield:

$$
\begin{aligned}
&\mathcal{U}(x,y,t) \\
&= \Phi_4(x,y,t,\zeta) + e^{-\lambda(\psi(t)-\psi(0))} \\
&\quad \times \left(f(x,y) - f(0,y) - x\frac{\partial}{\partial x}f(x,y)\Big|_{x=0}\right. \\
&\quad - f(x,0) + f(0,0) + x\frac{\partial}{\partial x}f(x,0)\Big|_{x=0} \\
&\quad - y\left(\frac{\partial}{\partial y}f(x,y)\Big|_{y=0} - \frac{\partial}{\partial y}f(x,y)\Big|_{x=y=0}\right. \\
&\quad \left.\left. - x\frac{\partial^2}{\partial x \partial y}f(x,y)\Big|_{x=y=0}\right)\right) \\
&\quad + h_1(x,t) - h_1(0,t) - x\frac{\partial}{\partial x}h_1(x,t)\Big|_{x=0} \\
&\quad + y\left(h_2(x,t) - h_2(0,t) - x\frac{\partial}{\partial x}h_2(x,t)\Big|_{x=0}\right. \\
&\quad - \Phi_4(x,1,t,\zeta) - e^{-\lambda(\psi(t)-\psi(0))} \\
&\quad \times \left(f(x,1) - f(0,1) - x\frac{\partial}{\partial x}f(x,1)\Big|_{x=0}\right. \\
&\quad - f(x,0) + f(0,0) \\
&\quad + x\frac{\partial}{\partial x}f(x,0)\Big|_{x=0} - \frac{\partial}{\partial y}f(x,y)\Big|_{y=0} \\
&\quad + \frac{\partial}{\partial y}f(x,y)\Big|_{x=y=0} \\
&\quad \left. + x\frac{\partial^2}{\partial x \partial y}f(x,y)\Big|_{x=y=0}\right) \\
&\quad \left. - h_1(x,t) + h_1(0,t) + x\frac{\partial}{\partial x}h_1(x,t)\Big|_{x=0}\right) \\
&\quad + g_1(y,t) + x\frac{\partial}{\partial x}\mathcal{U}(x,y,t)\Big|_{x=0} \\
&= \mathcal{U}^*(x,y,t).
\end{aligned} \tag{27}
$$

Utilizing the operator $\mathcal{I}_x^2$ to both sides of Equation (19) produces the following formulation:

$$
\begin{aligned}
\frac{\partial^{2+\zeta}}{\partial y^2 \partial t^\zeta}\mathcal{U}(x,y,t) &= \Phi_5(x,y,t) + \frac{\partial^{2+\zeta}}{\partial y^2 \partial t^\zeta}g_1(y,t) \\
&\quad + x\left(\frac{\partial}{\partial x}\frac{\partial^{2+\zeta}}{\partial y^2 \partial t^\zeta}\mathcal{U}(x,y,t)\right)\Bigg|_{x=0}.
\end{aligned} \tag{28}
$$

Evaluating Equation (28) at $x = 1$ yields the expression for $(\frac{\partial}{\partial x}\frac{\partial^{2+\zeta}}{\partial y^2 \partial t^\zeta}\mathcal{U}(x,y,t))|_{x=0}$ as follows:

$$
\begin{aligned}
&\left(\frac{\partial}{\partial x}\frac{\partial^{2+\zeta}}{\partial y^2 \partial t^\zeta}\mathcal{U}(x,y,t)\right)\Bigg|_{x=0} \\
&\quad = \frac{\partial^{2+\zeta}}{\partial y^2 \partial t^\zeta}g_2(y,t) - \Phi_5(1,y,t) \\
&\quad - \frac{\partial^{2+\zeta}}{\partial y^2 \partial t^\zeta}g_1(y,t).
\end{aligned} \tag{29}
$$

The combination of Equations (28) and (29) produces the subsequent expression:

$$
\begin{aligned}
&\frac{\partial^{2+\zeta}}{\partial y^2 \partial t^\zeta}\mathcal{U}(x,y,t) \\
&\quad = \Phi_5(x,y,t) + \frac{\partial^{2+\zeta}}{\partial y^2 \partial t^\zeta}g_1(y,t) \\
&\quad + x\left(\frac{\partial^{2+\zeta}}{\partial y^2 \partial t^\zeta}g_2(y,t) - \Phi_5(1,y,t)\right. \\
&\quad \left. - \frac{\partial^{2+\zeta}}{\partial y^2 \partial t^\zeta}g_1(y,t)\right).
\end{aligned} \tag{30}
$$

The application of $\mathcal{I}_y^2$ on both sides of Equation (30) yields the following formulation:

$$
\begin{aligned}
&\frac{\partial^\zeta}{\partial t^\zeta}\mathcal{U}(x,y,t) \\
&\quad = \Phi_6(x,y,t) + \frac{\partial^\zeta}{\partial t^\zeta}g_1(y,t) - \frac{\partial^\zeta}{\partial t^\zeta}g_1(0,t) \\
&\quad - y\frac{\partial^{1+\zeta}}{\partial y \partial t^\zeta}g_1(y,t)\Big|_{y=0} \\
&\quad + x\left(\frac{\partial^\zeta}{\partial t^\zeta}g_2(y,t) - \frac{\partial^\zeta}{\partial t^\zeta}g_2(0,t)\right. \\
&\quad - y\frac{\partial^{1+\zeta}}{\partial y \partial t^\zeta}g_2(y,t)\Big|_{y=0} - \Phi_6(1,y,t) \\
&\quad - \frac{\partial^\zeta}{\partial t^\zeta}g_1(y,t) + \frac{\partial^\zeta}{\partial t^\zeta}g_1(0,t) \\
&\quad \left. + y\frac{\partial^{1+\zeta}}{\partial y \partial t^\zeta}g_1(y,t)\Big|_{y=0}\right)
\end{aligned}
$$

$$+ \frac{\partial^\zeta}{\partial t^\zeta} h_1(x,t) + y\frac{\partial}{\partial y}\left(\frac{\partial^\zeta}{\partial t^\zeta}\mathcal{U}(x,y,t)\right)\Big|_{y=0}. \tag{31}$$

Setting $y = 1$ in Equation (31), we obtain the following expression for $\frac{\partial}{\partial y}(\frac{\partial^\zeta}{\partial t^\zeta}\mathcal{U}(x,y,t))|_{y=0}$:

$$\begin{aligned}\frac{\partial}{\partial y}\left(\frac{\partial^\zeta}{\partial t^\zeta}\mathcal{U}(x,y,t)\right)\Big|_{y=0} &= \frac{\partial^\zeta}{\partial t^\zeta}h_2(x,t) - \Phi_6(x,1,t) - \frac{\partial^\zeta}{\partial t^\zeta}g_1(1,t) \\ &+ \frac{\partial^\zeta}{\partial t^\zeta}g_1(0,t) + \frac{\partial^{1+\zeta}}{\partial y\partial t^\zeta}g_1(y,t)\Big|_{y=0} \\ &- x\left(\frac{\partial^\zeta}{\partial t^\zeta}g_2(1,t) - \frac{\partial^\zeta}{\partial t^\zeta}g_2(0,t)\right. \\ &- \frac{\partial^{1+\zeta}}{\partial y\partial t^\zeta}g_2(y,t)\Big|_{y=0} - \Phi_6(1,1,t) \\ &- \frac{\partial^\zeta}{\partial t^\zeta}g_1(1,t) + \frac{\partial^\zeta}{\partial t^\zeta}g_1(0,t) \\ &\left.+ \frac{\partial^{1+\zeta}}{\partial y\partial t^\zeta}g_1(y,t)\Big|_{y=0}\right) - \frac{\partial^\zeta}{\partial t^\zeta}h_1(x,t).\end{aligned} \tag{32}$$

Combining of Equations (31) and (32), we achieve:

$$\begin{aligned}\frac{\partial^\zeta}{\partial t^\zeta}\mathcal{U}(x,y,t) &= \Phi_6(x,y,t) + \frac{\partial^\zeta}{\partial t^\zeta}g_1(y,t) - \frac{\partial^\zeta}{\partial t^\zeta}g_1(0,t) \\ &- y\frac{\partial^{1+\zeta}}{\partial y\partial t^\zeta}g_1(y,t)\Big|_{y=0} \\ &+ x\left(\frac{\partial^\zeta}{\partial t^\zeta}g_2(y,t) - \frac{\partial^\zeta}{\partial t^\zeta}g_2(0,t)\right. \\ &- y\frac{\partial^{1+\zeta}}{\partial y\partial t^\zeta}g_2(y,t)\Big|_{y=0} - \Phi_6(1,y,t) \\ &- \frac{\partial^\zeta}{\partial t^\zeta}g_1(y,t) + \frac{\partial^\zeta}{\partial t^\zeta}g_1(0,t) \\ &\left.+ y\frac{\partial^{1+\zeta}}{\partial y\partial t^\zeta}g_1(y,t)\Big|_{y=0}\right) + \frac{\partial^\zeta}{\partial t^\zeta}h_1(x,t) \\ &+ y\left(\frac{\partial^\zeta}{\partial t^\zeta}h_2(x,t) - \Phi_6(x,1,t) - \frac{\partial^\zeta}{\partial t^\zeta}g_1(1,t)\right. \\ &+ \frac{\partial^\zeta}{\partial t^\zeta}g_1(0,t) + \frac{\partial^{1+\zeta}}{\partial y\partial t^\zeta}g_1(y,t)\Big|_{y=0} \\ &- x\left(\frac{\partial^\zeta}{\partial t^\zeta}g_2(1,t) - \frac{\partial^\zeta}{\partial t^\zeta}g_2(0,t)\right. \\ &- \frac{\partial^{1+\zeta}}{\partial y\partial t^\zeta}g_2(y,t)\Big|_{y=0} - \Phi_6(1,1,t) \\ &- \frac{\partial^\zeta}{\partial t^\zeta}g_1(1,t) + \frac{\partial^\zeta}{\partial t^\zeta}g_1(0,t) \\ &\left.\left.+ \frac{\partial^{1+\zeta}}{\partial y\partial t^\zeta}g_1(y,t)\Big|_{y=0}\right) - \frac{\partial^\zeta}{\partial t^\zeta}h_1(x,t)\right) \\ &= {}^{TC}D_{\psi}^{\zeta,\lambda}\mathcal{U}^*(x,y,t).\end{aligned} \tag{33}$$

Taking the integer-order integral operator $\mathcal{I}_x$ to both sides of Equation (27), we obtain:

$$\begin{aligned}\frac{\partial}{\partial x}\mathcal{U}(x,y,t) &= \Phi_7(x,y,t,\zeta) + e^{-\lambda(\psi(t)-\psi(0))} \\ &\times\left(\frac{\partial}{\partial x}f(x,y) - \frac{\partial}{\partial x}f(x,y)\Big|_{x=0} - \frac{\partial}{\partial x}f(x,0)\right. \\ &+ \frac{\partial}{\partial x}f(x,0)\Big|_{x=0} - y\left(\frac{\partial}{\partial x}\frac{\partial}{\partial y}f(x,y)\Big|_{y=0}\right. \\ &\left.\left.- \frac{\partial^2}{\partial x\partial y}f(x,y)\Big|_{x=y=0}\right)\right) \\ &+ \frac{\partial}{\partial x}h_1(x,t) - \frac{\partial}{\partial x}h_1(x,t)\Big|_{x=0} \\ &+ y\left(\frac{\partial}{\partial x}h_2(x,t) - h_2(0,t) - \frac{\partial}{\partial x}h_2(x,t)\Big|_{x=0}\right. \\ &- \Phi_7(x,1,t,\zeta) - e^{-\lambda(\psi(t)-\psi(0))} \\ &\times\left(\frac{\partial}{\partial x}f(x,1) - \frac{\partial}{\partial x}f(x,1)\Big|_{x=0} - \frac{\partial}{\partial x}f(x,0)\right. \\ &+ \frac{\partial}{\partial x}f(x,0)\Big|_{x=0} - \frac{\partial}{\partial x}\frac{\partial}{\partial y}f(x,y)\Big|_{y=0} \\ &\left.+ \frac{\partial^2}{\partial x\partial y}f(x,y)\Big|_{x=y=0}\right) \\ &\left.- \frac{\partial}{\partial x}h_1(x,t) + \frac{\partial}{\partial x}h_1(x,t)\Big|_{x=0}\right) \\ &+ \frac{\partial}{\partial x}\left(x\frac{\partial}{\partial x}\mathcal{U}(x,y,t)\Big|_{x=0}\right) = \mathcal{U}_x^*(x,y,t).\end{aligned} \tag{34}$$

Based on Equations (4), (23), (26), (27), (33) and (34), we achieve:

$$\mathcal{V}(x,y,t) = {}^{TC}\mathcal{D}_{\psi,t}^{\zeta,\lambda}\mathcal{U}^*(x,y,t) - a_1\mathcal{U}_{xx}^*(x,y,t)$$

$$\begin{aligned}&- a_2\mathcal{U}^*_{yy}(x,y,t)\\&- a_3\mathcal{U}^*_x(x,y,t) - \mathcal{F}(x,y,t,\mathcal{U}^*)\\&= \mathcal{V}^*(x,y,t).\end{aligned} \tag{35}$$

By substituting Equations (27) and (35) in Equation (3), we get

$$\min \mathcal{J}[\mathcal{U}] = \int_0^1\int_0^1\int_0^1 \mathcal{G}(x,y,t,\mathcal{U}^*(x,y,t),\mathcal{V}^*(x,y,t))\,\mathrm{d}x\,\mathrm{d}y\,\mathrm{d}t. \tag{36}$$

The evaluation of the integral in (36) is carried out using the three-dimensional Legendre-Gauss quadrature rule as

$$\begin{aligned}\min \mathcal{J}^*[\mathcal{U}] = \frac{1}{8}\sum_{i=1}^{\tilde{n}}\sum_{j=1}^{\tilde{n}}\sum_{r=1}^{\tilde{n}} \varpi_i\varpi_j\varpi_r\\ \times \mathcal{G}\left(\frac{1+\xi_i}{2},\frac{1+\xi_j}{2},\frac{1+\xi_r}{2},\right.\\ \mathcal{U}^*\left(\frac{1+\xi_i}{2},\frac{1+\xi_j}{2},\frac{1+\xi_r}{2}\right),\\ \left.\mathcal{V}^*\left(\frac{1+\xi_i}{2},\frac{1+\xi_j}{2},\frac{1+\xi_r}{2}\right)\right),\end{aligned} \tag{37}$$

where $\xi_r, r = 1,2,\dots,\tilde{n}$ are zeros of the Legendre polynomial $P_{\tilde{n}}(t)$ and

$$\varpi_r = \frac{-2}{(\tilde{n}+1)P'_{\tilde{n}}(\xi_r)P_{\tilde{n}+1}(\xi_r)}, \qquad r = 1,2,\dots,\tilde{n}.$$

By obtaining the solution of the following algebraic system

$$\frac{\partial}{\partial u_{i,k}}\mathcal{J}^*[\mathcal{U}] = 0, \quad 0 \le i \le (m+1)^2 - 1, \quad 0 \le k \le \tilde{m}, \tag{38}$$

by employing iterative solvers such as Newton's method, the components $u_{i,k}$ of the matrix U are computed, yielding an optimal solution to the primary problem. The flowchart in Figure 1 illustrates the sequential steps of the proposed algorithm.

Remark 3.2: In a similar fashion, the proposed numerical method is developed for the 2D-ψ-TFOCP.

Remark 3.3: Because the deep Bernoulli neural network architecture and the ψ-tempered operators are smooth and continuously differentiable, the nonlinear mapping defined by the discretised optimality system is Fréchet differentiable and its Jacobian exists. The Gauss–Legendre discretization combined with the smooth Bernoulli basis embedded in the neural network results in a well-conditioned and nonsingular Jacobian matrix. Moreover, the discrete Hessian of the cost functional is positive definite due to the convexity of the regularisation term and the boundedness of the ψ-tempered operators. These analytical properties ensure that Newton's method is well-posed, locally convergent, and numerically stable for solving the resulting nonlinear system.

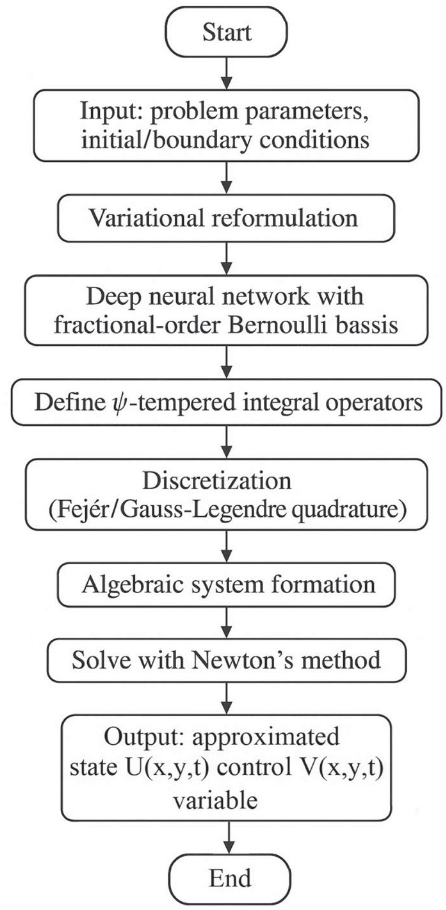

Figure 1. The flowchart of the proposed numerical method.

4. Error bound for the approximated cost function

In this section, we derive the error bound for the cost function obtained in Section 3 within the framework of Sobolev norms. For simplicity of analysis, we set $m = \tilde{m}$. The Sobolev norm on the domain $\Upsilon =$

$(0,1)^d \subset \mathbb{R}^d$, with $d \in \{2,3\}$ and $\mu \geq 1$, is expressed as follows Rahimkhani and Heydari (2023):

$$\| \mathcal{U} \|_{H^{\mu}(\Upsilon)}= \left(\sum_{j=0}^{\mu} \sum_{i=1}^{d} \| D_i^{(j)} \mathcal{U} \|^2_{L^2(\Upsilon)} \right)^{\frac{1}{2}}, \tag{39}$$

here $D_i^{(j)}$ denotes the j-th derivative of $\mathcal{U}$ with respect to the i-th variable, while the seminorm $|\mathcal{U}|_{H^{\mu;m}(\Upsilon)}$ is defined by:

$$|\mathcal{U}|_{H^{\mu;m}(\Upsilon)} = \left(\sum_{j=\min(\mu,m+1)}^{\mu} \sum_{i=1}^{d} \| D_i^{(j)} \mathcal{U} \|^2_{L^2(\Upsilon)} \right)^{\frac{1}{2}}.$$

Theorem 4.1 (Rahimkhani & Heydari, 2023): *Consider $\mathcal{U} \in H^{\mu}(\Upsilon)$ with $\mu \geq 0$ and $m \geq \mu$, and let $\mathcal{U}^*$ denote the best approximation of $\mathcal{U}$ obtained from the FBDNN. Under these assumptions, the error estimate is given by:*

$$\|\mathcal{U} - \mathcal{U}^*\|_{L^2(\Upsilon)} \leq c\varrho m^{-\mu}, \tag{40}$$

and for $1 \leq s \leq \mu$

$$\|\mathcal{U} - \mathcal{U}^*\|_{H^s(\Upsilon)} \leq c\varrho m^{2s-\frac{1}{2}-\mu}, \tag{41}$$

where c depends on μ. Also, we have

$$\left\| \frac{\partial^2}{\partial x^2}\mathcal{U}(x,y,t) - \frac{\partial^2}{\partial x^2}\mathcal{U}^*(x,y,t) \right\|_{L^2(\Upsilon)} \leq c\varrho m^{2s-\frac{1}{2}-\mu}, \tag{42}$$

$$\left\| \frac{\partial^2}{\partial y^2}\mathcal{U}(x,y,t) - \frac{\partial^2}{\partial y^2}\mathcal{U}^*(x,y,t) \right\|_{L^2(\Upsilon)} \leq c\varrho m^{2s-\frac{1}{2}-\mu}, \tag{43}$$

and

$$\left\| \frac{\partial}{\partial x}\mathcal{U}(x,y,t) - \frac{\partial}{\partial x}\mathcal{U}^*(x,y,t) \right\|_{L^2(\Upsilon)} \leq c\varrho m^{2s-\frac{1}{2}-\mu}, \tag{44}$$

where

$$1 \leq s \leq \mu, \quad \varrho = |\mathcal{U}|_{H^{\mu;m}(\Upsilon)}.$$

Remark 4.1: It follows from the theoretical results in Mashayekhi et al. (2016) and Canuto et al. (2006) that the Sobolev error

$$\|\mathcal{U} - \mathcal{U}^*\|_{L^2(\Upsilon)} = O\left(m^{-(\mu+\frac{1}{2}-2s)}\right),$$

provided that $2s - \frac{1}{2} < \mu$. Hence, as $m \to \infty$, the approximation converges to $\mathcal{U}^*$; in the case of infinitely smooth $\mathcal{U}$, the convergence rate exceeds any algebraic order of $\frac{1}{m}$.

Theorem 4.2: *Suppose that $\mathcal{U}$ is an absolutely ψ-integrable function defined over the domain Υ, and $\lambda > 0$. Under these assumptions, the following result is obtained:*

$$\begin{aligned} &\|{}^T\mathcal{I}^{\zeta,\lambda}_{\psi,t}\mathcal{U}(x,y,t) - {}^T\mathcal{I}^{\zeta,\lambda}_{\psi,t}\mathcal{U}^*(x,y,t)\|_{L^2(\Upsilon)} \\ &\quad \leq \delta_1 \|\mathcal{U} - \mathcal{U}^*\|_{L^2(\Upsilon)}, \end{aligned} \tag{45}$$

where

$$\delta_1 = \ell \frac{(\psi(1) - \psi(0))^{\zeta}}{\Gamma(\zeta+1)},$$

and

$$\|\mathcal{U} - \mathcal{U}^*\|_{L^{\infty}(\Upsilon)} \leq \ell \|\mathcal{U} - \mathcal{U}^*\|_{L^2(\Upsilon)}.$$

Proof: Using the non-decreasing property of the function ψ on the domain Υ, the following result is derived:

$$\begin{aligned} &|{}^T\mathcal{I}^{\zeta,\lambda}_{\psi,t}\mathcal{U}(x,y,t) - {}^T\mathcal{I}^{\zeta,\lambda}_{\psi,t}\mathcal{U}^*(x,y,t)| \\ &\quad \leq \frac{1}{\Gamma(\zeta)} \int_0^t \psi'(s)(\psi(t) - \psi(s))^{\zeta-1} e^{-\lambda(\psi(t)-\psi(s))} \\ &\quad \times |\mathcal{U}(x,y,s) - \mathcal{U}^*(x,y,s)|\, \mathrm{d}s \\ &\quad \leq \frac{1}{\Gamma(\zeta)} \int_0^t \psi'(s)(\psi(t) - \psi(s))^{\zeta-1} e^{-\lambda(\psi(t)-\psi(t))} \\ &\quad \times |\mathcal{U}(x,y,s) - \mathcal{U}^*(x,y,s)|\, \mathrm{d}s \\ &\quad \leq \|\mathcal{U} - \mathcal{U}^*\|_{L^{\infty}(\Upsilon)} \frac{1}{\Gamma(\zeta)} \\ &\quad \times \int_0^t \psi'(s)(\psi(t) - \psi(s))^{\zeta-1}\, \mathrm{d}s \\ &\quad \leq \|\mathcal{U} - \mathcal{U}^*\|_{L^{\infty}(\Upsilon)} \frac{(\psi(t) - \psi(0))^{\zeta}}{\Gamma(\zeta+1)} \\ &\quad \leq \|\mathcal{U} - \mathcal{U}^*\|_{L^{\infty}(\Upsilon)} \frac{(\psi(1) - \psi(0))^{\zeta}}{\Gamma(\zeta+1)}. \end{aligned} \tag{46}$$

Applying the L_2−norm to both sides of Equation (46), yields the following relation:

$$\begin{aligned} &\|{}^T I^{\zeta,\lambda}_{\psi,t}\mathcal{U}(x,y,t) - {}^T I^{\zeta,\lambda}_{\psi,t}\mathcal{U}^*(x,y,t)\|_{L^2(\Upsilon)} \\ &\quad \leq \ell \frac{(\psi(1) - \psi(0))^{\zeta}}{\Gamma(\zeta+1)} \|\mathcal{U} - \mathcal{U}^*\|_{L^2(\Upsilon)}. \end{aligned} \tag{47}$$

■

Theorem 4.3: *Let us consider the assumptions of Theorems 4.1 and 4.2 hold, and let $\mathcal{U} \in AC^n_\psi(\Upsilon)$ with $0 < \zeta \le 1$, $\lambda > 0$. Accordingly, the following result is established:*

$$\|{}^{TC}\mathcal{D}^{\zeta,\lambda}_{\psi,t}\mathcal{U}(x,y,t) - {}^{TC}\mathcal{D}^{\zeta,\lambda}_{\psi,t}\mathcal{U}^*(x,y,t)\|_{L^2(\Upsilon)} \le \delta_2 \varrho m^{-\mu}, \tag{48}$$

where

$$\delta_2 = c\delta_1\left(Mm^{2s-\frac{1}{2}} + \lambda\right), \quad M = \left\|\frac{1}{\psi'}\right\|_{L^\infty([0,1])}.$$

In fact, M is the maximum of $\frac{1}{\psi'(t)}$ over $[0,1]$. In practice, this constant can be evaluated either analytically (when ψ is explicitly known) or numerically by sampling over a fine grid.

Proof: Utilizing Definition 2.2 with the restriction $0 < \zeta \le 1$, the following result is derived:

$$\begin{aligned}
&|{}^{TC}\mathcal{D}^{\zeta,\lambda}_{\psi,t}\mathcal{U}(x,y,t) - {}^{TC}\mathcal{D}^{\zeta,\lambda}_{\psi,t}\mathcal{U}^*(x,y,t)| \\
&= \left|{}^{T}\mathcal{I}^{\zeta,\lambda}_{\psi,t}\left(\frac{1}{\psi'(t)}.\frac{\partial}{\partial t} + \lambda\right)\mathcal{U}(x,y,t) \right.\\
&\quad \left. -{}^{T}\mathcal{I}^{\zeta,\lambda}_{\psi,t}\left(\frac{1}{\psi'(t)}.\frac{\partial}{\partial t} + \lambda\right)\mathcal{U}^*(x,y,t)\right| \\
&\le \left|{}^{T}\mathcal{I}^{\zeta,\lambda}_{\psi,t}\left(\frac{1}{\psi'(t)}\frac{\partial}{\partial t}\mathcal{U}(x,y,t) + \lambda\mathcal{U}(x,y,t)\right) \right.\\
&\quad \left. -{}^{T}\mathcal{I}^{\zeta,\lambda}_{\psi,t}\left(\frac{1}{\psi'(t)}\frac{\partial}{\partial t}\mathcal{U}^*(x,y,t) + \lambda\mathcal{U}^*(x,y,t)\right)\right| \\
&\le \left|{}^{T}\mathcal{I}^{\zeta,\lambda}_{\psi,t}\left(\frac{1}{\psi'(t)}\left(\frac{\partial}{\partial t}\mathcal{U}(x,y,t) - \frac{\partial}{\partial t}\mathcal{U}^*(x,y,t)\right)\right) \right.\\
&\quad \left. +\lambda\,{}^{T}\mathcal{I}^{\zeta,\lambda}_{\psi,t}(\mathcal{U}(x,y,t) - \mathcal{U}^*(x,y,t))\right|.
\end{aligned} \tag{49}$$

By applying L_2-norm to both sides of Equation (49) and invoking Theorems 4.1 and 4.2, we achieve

$$\begin{aligned}
&\|{}^{TC}\mathcal{D}^{\zeta,\lambda}_{\psi,t}\mathcal{U}(x,y,t) - {}^{TC}\mathcal{D}^{\zeta,\lambda}_{\psi,t}\mathcal{U}^*(x,y,t)\|_{L^2(\Upsilon)} \\
&\quad \le M\left\|{}^{T}\mathcal{I}^{\zeta,\lambda}_{\psi,t}\left(\frac{\partial}{\partial t}\mathcal{U}(x,y,t) - \frac{\partial}{\partial t}\mathcal{U}^*(x,y,t)\right)\right\|_{L^2(\Upsilon)} \\
&\qquad + \lambda\|{}^{T}\mathcal{I}^{\zeta,\lambda}_{\psi,t}(\mathcal{U}(x,y,t) - \mathcal{U}^*(x,y,t))\|_{L^2(\Upsilon)} \\
&\le M\delta_1\left\|\frac{\partial}{\partial t}\mathcal{U}(x,y,t) - \frac{\partial}{\partial t}\mathcal{U}^*(x,y,t)\right\|_{L^2(\Upsilon)} \\
&\qquad + \lambda\delta_1\|\mathcal{U}(x,y,t) - \mathcal{U}^*(x,y,t)\|_{L^2(\Upsilon)} \\
&\le c\delta_1\varrho\left(Mm^{2s-\frac{1}{2}} + \lambda\right)m^{-\mu}.
\end{aligned} \tag{50}$$

■

Theorem 4.4: *Suppose the assumptions of Theorems 4.1–4.3 are satisfied, and that the function $\mathcal{F}$ fulfills the Lipschitz condition with constant κ_1. Then, it follows that:*

$$\begin{aligned}
&\|\mathcal{V}(x,y,t) - \mathcal{V}^*(x,y,t)\|_{L^2(\Upsilon)} \\
&\quad \le c\varrho(\delta_1(Mm^{2s-\frac{1}{2}} + \lambda) \\
&\qquad + (a_1 + a_2 + a_3)m^{2s-\frac{1}{2}} + \kappa_1)m^{-\mu}.
\end{aligned} \tag{51}$$

Proof: From Equations (35), (40), (42)–(44) and (48), we conclude

$$\begin{aligned}
&\|\mathcal{V}(x,y,t) - \mathcal{V}^*(x,y,t)\|_{L^2(\Upsilon)} \\
&= \|{}^{TC}\mathcal{D}^{\zeta,\lambda}_{\psi,t}\mathcal{U}(x,y,t) - a_1\mathcal{U}_{xx}(x,y,t) \\
&\quad - a_2\mathcal{U}_{yy}(x,y,t) - a_3\mathcal{U}_x(x,y,t) \\
&\quad - \mathcal{F}(x,y,t,\mathcal{U}) - {}^{TC}\mathcal{D}^{\zeta,\lambda}_{\psi,t}\mathcal{U}^*(x,y,t) \\
&\quad + a_1\mathcal{U}^*_{xx}(x,y,t) + a_2\mathcal{U}^*_{yy}(x,y,t) \\
&\quad + a_3\mathcal{U}^*_x(x,y,t) + \mathcal{F}(x,y,t,\mathcal{U}^*)\|_{L^2(\Upsilon)} \\
&\le \|{}^{TC}\mathcal{D}^{\zeta,\lambda}_{\psi,t}\mathcal{U}(x,y,t) - {}^{TC}\mathcal{D}^{\zeta,\lambda}_{\psi,t}\mathcal{U}^*(x,y,t)\|_{L^2(\Upsilon)} \\
&\quad + a_1\|\mathcal{U}_{xx}(x,y,t) - \mathcal{U}^*_{xx}(x,y,t)\|_{L^2(\Upsilon)} \\
&\quad + a_2\|\mathcal{U}_{yy}(x,y,t) - \mathcal{U}^*_{yy}(x,y,t)\|_{L^2(\Upsilon)} \\
&\quad + a_3\|\mathcal{U}_x(x,y,t) - \mathcal{U}^*_x(x,y,t)\|_{L^2(\Upsilon)} \\
&\quad + \kappa_1\|\mathcal{U}(x,y,t) - \mathcal{U}^*(x,y,t)\|_{L^2(\Upsilon)} \\
&\le c\delta_1\varrho(Mm^{2s-\frac{1}{2}} + \lambda)m^{-\mu} \\
&\quad + (a_1 + a_2 + a_3)c\varrho m^{2s-\frac{1}{2}-\mu} + \kappa_1 c\varrho m^{-\mu} \\
&= c\varrho\left(\delta_1\left(Mm^{2s-\frac{1}{2}} + \lambda\right) + (a_1 + a_2 + a_3)\right. \\
&\quad \left.\times\ m^{2s-\frac{1}{2}} + \kappa_1\right)m^{-\mu}.
\end{aligned} \tag{52}$$

■

Theorem 4.5: *Assuming the hypotheses of Theorems 4.1–4.4 hold, and that the function $\mathcal{G}$ satisfies the Lipschitz condition with constant κ_2, we obtain the following result:*

$$\begin{aligned}
&\|\mathcal{J}[\mathcal{U},\mathcal{V}] - \mathcal{J}[\mathcal{U}^*,\mathcal{V}^*]\|_{L^2(\Upsilon)} \\
&\quad \le c\varrho\kappa_2(1 + \delta_1(Mm^{2s-\frac{1}{2}} + \lambda) \\
&\qquad + (a_1 + a_2 + a_3)m^{2s-\frac{1}{2}} + \kappa_1)m^{-\mu}.
\end{aligned} \tag{53}$$

Proof: From Equations (3), (40) and (51), we get

$$\begin{aligned}
&\|\mathcal{J}[\mathcal{U},\mathcal{V}]-\mathcal{J}[\mathcal{U}^*,\mathcal{V}^*]\|_{L^2(\Upsilon)}\\
&\leq \left\|\int_0^1\int_0^1\int_0^1 \mathcal{G}(x,y,t,\mathcal{U}(x,y,t),\mathcal{V}(x,y,t))\right.\\
&\quad \left.-\mathcal{G}(x,y,t,\mathcal{U}^*(x,y,t),\mathcal{V}^*(x,y,t))\,\mathrm{d}x\,\mathrm{d}y\,\mathrm{d}t\right\|_{L^2(\Upsilon)}\\
&\leq \kappa_2\|\mathcal{U}(x,y,t)-\mathcal{U}^*(x,y,t)\|_{L^2(\Upsilon)}\\
&\quad +\kappa_2\|\mathcal{V}(x,y,t)-\mathcal{V}^*(x,y,t)\|_{L^2(\Upsilon)}\\
&\leq c\varrho\kappa_2(1+\delta_1(Mm^{2s-\frac{1}{2}}+\lambda)\\
&\quad +(a_1+a_2+a_3)m^{2s-\frac{1}{2}}+\kappa_1)m^{-\mu}. \qquad (54)
\end{aligned}$$

Therefore, the upper bound of the method's error is established ■

5. Numerical illustration

This section validates the proposed method by applying it to one 1D-ψ-TFOCPs, two 2D-ψ-TFOCPs and one 3D-ψ-TFOCPs, thereby providing a comprehensive assessment of its reliability and numerical precision.

The computations associated with the examples were performed using Mathematical 14. Also, we report the CPU time (seconds) in the examples, which have been obtained on a 2.4 GHz Core i7 personal computer with 16 GB of RAM.

The problem involves three key parameters: the fractional order ζ, the tempering index λ, and the kernel-generating function $\psi(t)$. The fractional order ζ controls the strength of non-local memory effects, where smaller values introduce stronger long-range dependence and $\zeta \to 1$ reproduces the classical (local) dynamics. The tempering index λ regulates the exponential decay of memory, with $\lambda = 0$ corresponding to the standard fractional model and larger values leading to short-memory behaviour. The function $\psi(t)$ defines the structure of the fractional kernel and enables modelling of systems with non-uniform temporal scaling. In our numerical examples, the specific values of ζ, λ, and $\psi(t)$ were carefully chosen to ensure a meaningful assessment of the proposed methodology. The fractional orders ζ were selected to represent a range of memory effects, from weak (near-local) to strong (highly nonlocal) behaviour, which allows us to examine the accuracy and stability of the method under different dynamical regimes. The tempering index λ values were selected to explore both the classical fractional behaviour ($\lambda = 0$) and various degrees of memory decay ($\lambda > 0$), highlighting the method's robustness across different levels of memory influence. Different forms of $\psi(t)$, including linear and nonlinear functions, were considered to represent diverse kernel structures and temporal scalings, reflecting potential applications in real-world systems with non-uniform memory effects. By varying these parameters systematically, we not only test the performance and flexibility of the ψ-tempered fractional framework but also demonstrate that the proposed method can handle a wide range of problem configurations, from classical to strongly non-local regimes.

Example 5.1: Consider the following 1D-ψ-TFOCPs:

$$\min \mathcal{J}[\mathcal{U},\mathcal{V}] = \int_0^1 (\mathcal{U}^2(t)+\mathcal{V}^2(t))\,\mathrm{d}t, \qquad (55)$$

subject to

$$\begin{aligned}
&{}^{TC}\mathcal{D}^{\zeta,\lambda}_{\psi,t}\mathcal{U}(t) = -\mathcal{U}(t)+\mathcal{V}(t), \quad 0<\zeta\leq 1, &(56)\\
&\mathcal{U}(0)=1. &(57)
\end{aligned}$$

For $\zeta = 1, \psi(t) = t, \lambda = 0$, the optimal values for $\mathcal{U}(t), \mathcal{V}(t)$ and $\mathcal{J}$ are

$$\begin{aligned}
\mathcal{U}(t) &= \cosh(\sqrt{2}t) - 0.98\sinh(\sqrt{2}t),\\
\mathcal{V}(t) &= (1-0.98\sqrt{2})\cosh(\sqrt{2}t)\\
&\quad + (\sqrt{2}-0.98)\sinh(\sqrt{2}t),\\
\mathcal{J} &= 0.192909.
\end{aligned}$$

In Table 1, we compare values of $\mathcal{J}$ by using the Variational iteration (Alizadeh & Effati, 2018), Adomian decomposition (Zeid & Yousefi, 2016), Legendre wavelets (Sahu & Saha Ray, 2018), Chebyshev wavelets (Sahu & Saha Ray, 2018), Laguerre wavelets (Sahu & Saha Ray, 2018), Cosine and sine wavelets (Sahu & Saha Ray, 2018), Legendre wavelets collocation (Kumar & Mehra, 2021), Bernstein wavelets (Rahimkhani & Ordokhani, 2021) method and the present method with $m = 1, \mathcal{N} = 1, \epsilon = 1.084, \psi(t) = t, \lambda = 0$. We report the computational time by using Legendre wavelets (Sahu & Saha Ray, 2018), Chebyshev wavelets (Sahu & Saha Ray, 2018), Laguerre wavelets (Sahu & Saha Ray, 2018), Cosine and sine wavelets (Sahu & Saha Ray, 2018),

Table 1. Comparison of $\mathcal{J}$ for $\psi(t) = t, \lambda = 0$ with results from other methods (Example 5.1).

Method	$\zeta = 0.8$	$\zeta = 0.9$	$\zeta = 0.99$	$\zeta = 1$
Variational iteration method	0.16711	0.17953	0.19153	0.192909
Adomian decomposition method	0.16740	0.17962	0.19155	0.192909
Legendre wavelets method	0.167078	0.179529	0.191531	0.192909
Chebyshev wavelets method	0.167328	0.179641	0.19155	0.192921
Laguerre wavelets method	0.181798	0.185942	0.19169	0.192604
Cosine and sine wavelets method	0.168072	0.180555	0.192572	0.196914
Legendre wavelets collocation method	0.167073	0.179543	0.191556	0.192935
Bernstein wavelets method	0.153519	0.169226	0.181852	0.183102
Presented method	0.169193	0.179970	0.191537	0.192909

Table 2. Comparison of Computational time for $\psi(t) = t, \lambda = 0$ with results from other methods (Example 5.1).

Method	$\zeta = 0.8$	$\zeta = 0.9$	$\zeta = 0.99$	$\zeta = 1$
Legendre wavelets method	4.868	18.408	18.034	17.94
Chebyshev wavelets method	17.534	677.699	677.559	661.069
Laguerre wavelets method	4.963	57.361	56.971	56.128
Cosine and sine wavelets method	153.287	1884.63	1331.66	1103.05
Presented method	0.015	0.016	0.016	0.001

and our method in Table 2. From these tables, it may be concluded that the presented method gives better results than other methods for this problem.

Example 5.2: Consider the following 2D-ψ-TFOCPs:

$$\min \mathcal{J}[\mathcal{U},\mathcal{V}] = \int_0^1 \int_0^1 (e^{-t}(e^{-\lambda\psi(t)}(\psi(t)-\psi(0))^6 \times \sin(x) - \mathcal{U}(x,t))^2 + e^x(e^{-\lambda\psi(t)}(\psi(t)-\psi(0))^5\cos(x) - \mathcal{V}(x,t))^2)\,dx\,dt, \tag{58}$$

under the following constraint

$$\begin{cases} {}^{TC}\mathcal{D}^{\zeta,\lambda}_{\psi,t}\mathcal{U}(x,t) = 2\mathcal{U}_x(x,t) + \mathcal{U}_{xx}(x,t) + e^{-\mathcal{U}(x,t)} \\ \quad + \mathcal{V}(x,t) + \mathcal{F}(x,t), \\ \mathcal{U}(x,0) = 0, \quad 0 < x \leq 1, \\ \mathcal{U}(0,t) = 0, \quad \mathcal{U}(1,t) = e^{-\lambda\psi(t)}(\psi(t)-\psi(0))^6 \\ \quad \times \sin(1), \quad 0 < t \leq 1. \end{cases} \tag{59}$$

The exact solution corresponding to the aforementioned problem is given by:

$$\langle \mathcal{U}(x,t), \mathcal{V}(x,t), \mathcal{J}\rangle = \Big\langle e^{-\lambda\psi(t)}(\psi(t)-\psi(0))^6\sin(x), e^{-\lambda\psi(t)}(\psi(t)-\psi(0))^5\cos(x), 0\Big\rangle.$$

The approach described in Section 3 is implemented with $m = \tilde{m} = 2$, and $\epsilon_1 = \epsilon_2 = \frac{1}{5}$. Table 3 reports the numerical solutions of $\mathcal{U}$, denoted by $N_{\mathcal{U}}$, together with their corresponding absolute errors, denoted by $AE_{\mathcal{U}}$, for the case $\zeta = 0.95$, $\mathcal{N} = 2$, and $\psi(t) = t$, evaluated over various values of λ. The table clearly demonstrates that the proposed method yields highly accurate results with small basis. Table 4 presents the $AE_{\mathcal{U}}$ and the absolute errors of $\mathcal{V}$ denoted by $AE_{\mathcal{V}}$ corresponding to $\zeta = 0.95$, $\mathcal{N} = 3$, and $\lambda = 3$. The outcomes are presented for various selections of the function ψ, thereby illustrating the impact of ψ on the accuracy of the proposed method. Moreover, these tables include the corresponding values of the cost function and computational time. To investigate the influence of the parameter ζ and function $\psi(t)$, the 2D-plots of $\mathcal{U}$ and $\mathcal{V}$ corresponding to $\mathcal{N} = 2$ and $\lambda = 3$ in $x = 0.25$ are presented in Figure 2. Figure 3 illustrates the density distributions of the numerical and exact solutions, together with their corresponding absolute errors, for the case $\zeta = 0.75$, $\mathcal{N} = 2$, $\lambda = 1$, and $\psi(t) = \sinh(t)$. The comparison highlights the accuracy and reliability of the proposed method under the given parameter settings. Figure 4 shows the 3D-plot of the numerical solutions and absolute errors of $\mathcal{U}$ and $\mathcal{V}$ with $\mathcal{N} = 2$, and $\lambda = 3$.

Example 5.3: Consider the following 2D-ψ-TFOCPs:

$$\min \mathcal{J}[\mathcal{U},\mathcal{V}] = \int_0^1 \int_0^1 (\sin(t)(e^{-\lambda\psi(t)}(\psi(t)-\psi(0))^4 e^{-x}$$

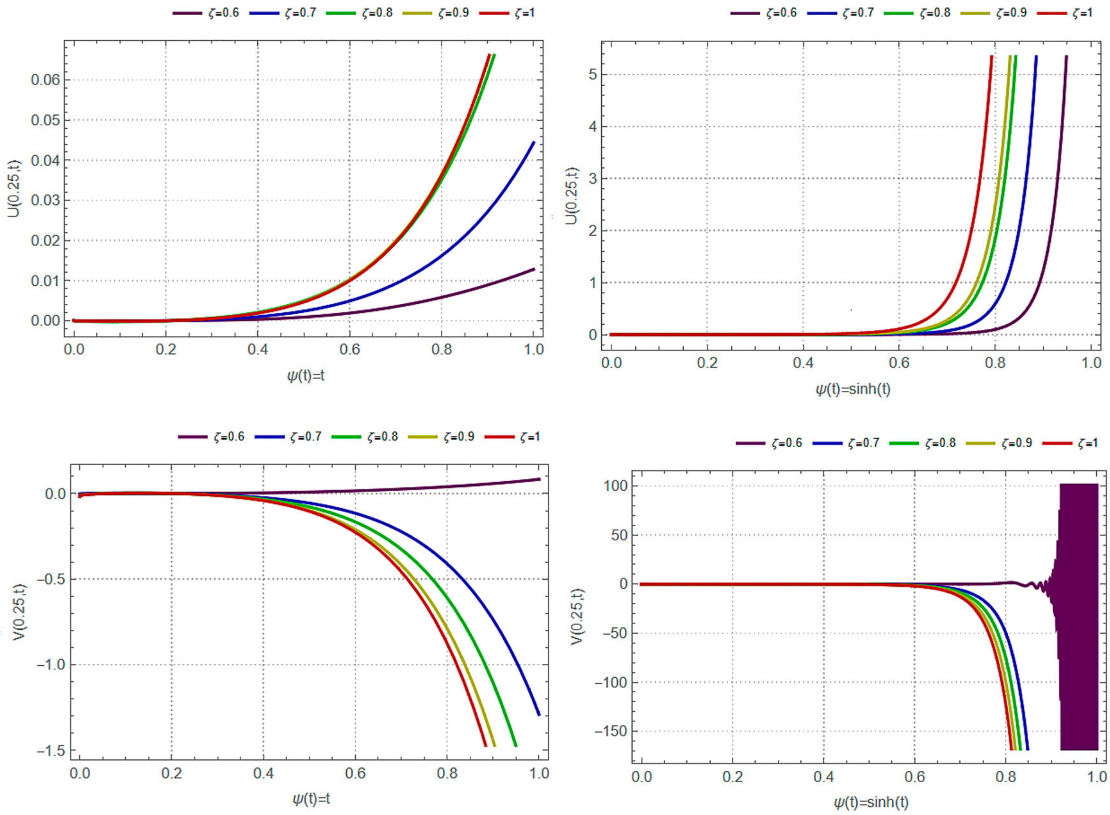

Figure 2. The numerical solutions with $\mathcal{N} = 2$, and $\lambda = 3$ (Example 5.2).

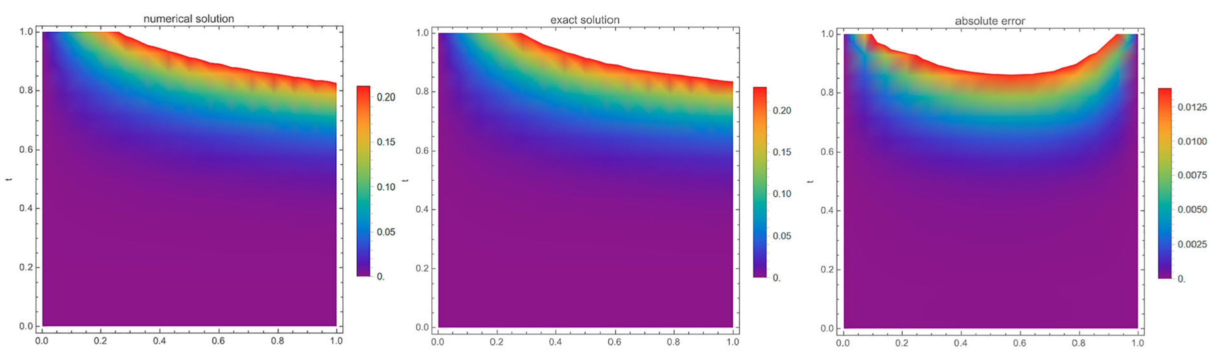

Figure 3. The density distributions of numerical, exact solutions and their absolute errors with $\zeta = 0.75, \mathcal{N} = 2, \lambda = 1$ and $\psi(t) = \sinh(t)$ (Example 5.2).

Table 3. The $N_{\mathcal{U}}$ and $AE_{\mathcal{U}}$ for $\zeta = 0.95, \mathcal{N} = 2$ and $\psi(t) = t$ (Example 5.2).

	$\lambda = 0$		$\lambda = 1$		$\lambda = 3$		$\lambda = 5$	
(x, t)	$N_{\mathcal{U}}$	$AE_{\mathcal{U}}$	$N_{\mathcal{U}}$	$AE_{\mathcal{U}}$	$N_{\mathcal{U}}$	$AE_{\mathcal{U}}$	$N_{\mathcal{U}}$	$AE_{\mathcal{U}}$
(0.1, 0.1)	0.000000	2.92×10^{-6}	0.000000	2.41×10^{-6}	0.000000	1.60×10^{-6}	0.000000	1.02×10^{-6}
(0.2, 0.2)	0.000012	8.29×10^{-7}	0.000013	2.47×10^{-6}	0.000016	8.67×10^{-6}	0.000020	1.51×10^{-5}
(0.3, 0.3)	0.000201	1.40×10^{-5}	0.000164	4.79×10^{-6}	0.000132	4.43×10^{-5}	0.000146	9.83×10^{-5}
(0.4, 0.4)	0.001423	1.72×10^{-4}	0.000996	7.28×10^{-5}	0.000588	1.08×10^{-4}	0.000594	3.78×10^{-4}
(0.5, 0.5)	0.006653	8.38×10^{-4}	0.004122	4.22×10^{-4}	0.001869	1.98×10^{-4}	0.001776	1.16×10^{-3}
(0.6, 0.6)	0.023667	2.68×10^{-3}	0.013133	1.32×10^{-3}	0.004684	3.29×10^{-4}	0.004364	3.05×10^{-3}
(0.7, 0.7)	0.069431	6.36×10^{-3}	0.034680	2.96×10^{-3}	0.009825	5.44×10^{-4}	0.009222	6.93×10^{-3}
(0.8, 0.8)	0.176600	1.14×10^{-2}	0.079583	4.91×10^{-3}	0.017916	8.56×10^{-4}	0.016604	1.31×10^{-2}
(0.9, 0.9)	0.402565	1.37×10^{-2}	0.163858	5.39×10^{-3}	0.028999	1.02×10^{-3}	0.022488	1.79×10^{-2}
$\mathcal{J}$	7.95956×10^{-9}		2.34075×10^{-9}		7.55457×10^{-9}		5.14139×10^{-8}	
CPU	3.188		3.235		3.437		3.125	

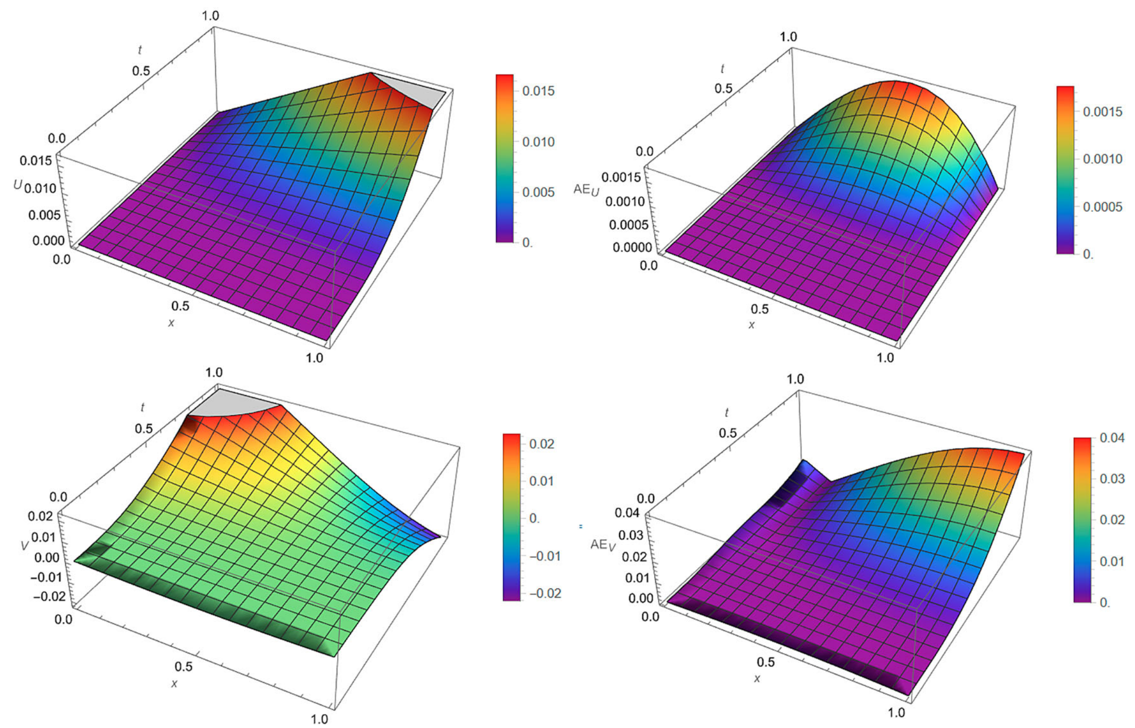

Figure 4. The numerical solutions and their corresponding absolute errors with $\zeta = 0.95, \mathcal{N} = 2, \lambda = 3$ and $\psi(t) = \sin(t)$ (Example 5.2).

Table 4. The $AE_{\mathcal{U}}$ and $AE_{\mathcal{V}}$ for $\zeta = 0.95, \mathcal{N} = 3$ and $\lambda = 3$ (Example 5.2).

	$\psi(t) = t$		$\psi(t) = \sinh(t)$		$\psi(t) = \sin(t)$	
(x, t)	$AE_{\mathcal{U}}$	$AE_{\mathcal{V}}$	$AE_{\mathcal{U}}$	$AE_{\mathcal{V}}$	$AE_{\mathcal{U}}$	$AE_{\mathcal{V}}$
$(0.1, 0.1)$	1.60×10^{-6}	2.30×10^{-6}	1.64×10^{-6}	1.44×10^{-6}	1.56×10^{-6}	2.84×10^{-6}
$(0.2, 0.2)$	8.68×10^{-6}	1.37×10^{-4}	1.16×10^{-5}	1.60×10^{-4}	6.21×10^{-6}	1.18×10^{-4}
$(0.3, 0.3)$	4.43×10^{-5}	4.29×10^{-5}	7.73×10^{-5}	9.94×10^{-5}	2.22×10^{-5}	9.20×10^{-6}
$(0.4, 0.4)$	1.08×10^{-4}	9.80×10^{-4}	3.30×10^{-4}	1.18×10^{-3}	9.39×10^{-6}	8.28×10^{-4}
$(0.5, 0.5)$	1.98×10^{-4}	4.21×10^{-3}	1.44×10^{-3}	7.33×10^{-3}	9.41×10^{-5}	3.01×10^{-3}
$(0.6, 0.6)$	3.30×10^{-4}	1.16×10^{-2}	7.10×10^{-3}	3.83×10^{-2}	3.14×10^{-4}	7.05×10^{-3}
$(0.7, 0.7)$	5.46×10^{-4}	2.58×10^{-2}	4.08×10^{-2}	2.66×10^{-1}	5.81×10^{-4}	1.32×10^{-2}
$(0.8, 0.8)$	8.59×10^{-4}	5.06×10^{-2}	2.87×10^{-1}	2.92×10^{0}	7.38×10^{-4}	2.12×10^{-2}
$\mathcal{J}$	7.83132×10^{-9}		1.53362×10^{-8}		3.45994×10^{-9}	
CPU	6.297		6.156		5.234	

$$
- \mathcal{U}(x,t))^2 + e^x \left(e^{-\lambda\psi(t)} (\psi(t) - \psi(0))^3 \times \sin\left(\frac{\pi}{2}x\right) - \mathcal{V}(x,t))^2 \right) \mathrm{d}x\,\mathrm{d}t, \tag{60}
$$

under the following constraint

$$
\begin{cases}
{}^{TC}\mathcal{D}^{\zeta,\lambda}_{\psi,t}\mathcal{U}(x,t) = \mathcal{U}_x(x,t) - \mathcal{U}_{xx}(x,t) \\
\quad + \sin(\mathcal{U}(x,t)) + \mathcal{V}(x,t) + \mathcal{F}(x,t), \\
\mathcal{U}(x,0) = 0, \quad 0 < x \le 1, \\
\mathcal{U}(0,t) = e^{-\lambda\psi(t)}(\psi(t) - \psi(0))^4, \\
\mathcal{U}(1,t) = e^{-\lambda\psi(t)}(\psi(t) - \psi(0))^4 e^{-1}, \quad 0 < t \le 1.
\end{cases} \tag{61}
$$

The exact solution corresponding to the aforementioned problem is given by:

$$
\begin{aligned}
&\langle \mathcal{U}(x,t), \mathcal{V}(x,t), \mathcal{J} \rangle \\
&= \Big\langle e^{-\lambda\psi(t)}(\psi(t) - \psi(0))^4 e^{-x}, e^{-\lambda\psi(t)} \\
&\quad \times (\psi(t) - \psi(0))^3 \sin\left(\frac{\pi}{2}x\right), 0 \Big\rangle.
\end{aligned}
$$

The approach described in Section 3 is implemented with $m = \tilde{m} = 2$, and $\epsilon_1 = \epsilon_2 = \frac{1}{5}$. Table 5 reports the numerical solutions of $\mathcal{U}$ and their corresponding absolute errors for the case $\zeta = 0.95, \mathcal{N} = 2$, and $\psi(t) = t$, evaluated over varying values of λ. Table 6 presents the absolute errors $\mathcal{U}$ and $\mathcal{V}$ for the case

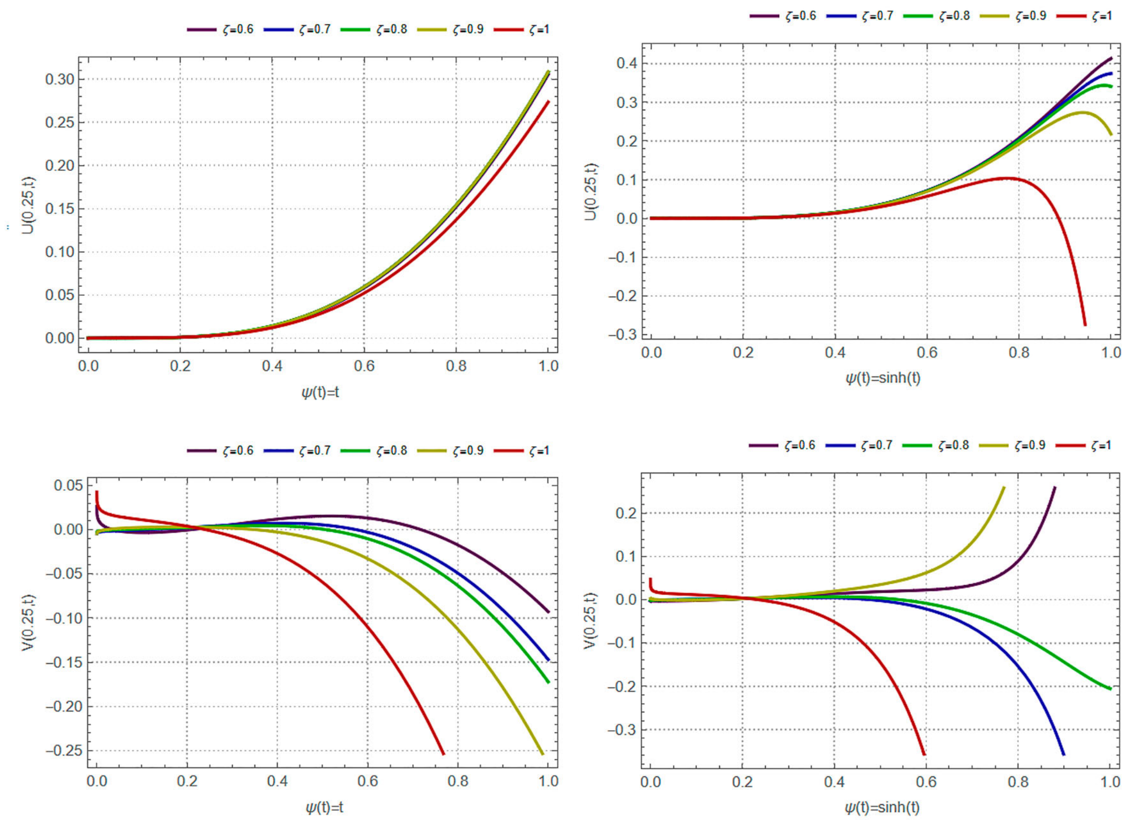

Figure 5. The numerical solutions with $\mathcal{N}=2$, and $\lambda=1$ (Example 5.3).

$\zeta=0.95$, $\mathcal{N}=3$, and $\lambda=1$, computed under different choices of the function ψ. The results highlight the sensitivity of the proposed method to the selection of ψ and emphasise its significant impact on solution accuracy. To further examine the effect of ζ and $\psi(t)$, Figure 5 displays two-dimensional plots of $\mathcal{U}$ and $\mathcal{V}$ for $\mathcal{N}=2$ and $\lambda=1$ at $x=0.25$. Figure 6 illustrates the density distributions of both numerical and exact solutions, along with their associated absolute errors, for $\zeta=0.75$, $\mathcal{N}=2$, $\lambda=3$, and $\psi(t)=\sin(t)$. The comparison emphasises the precision and robustness of the proposed methodology under these parameter settings. Figure 7 presents the three-dimensional visualisation of the numerical solutions and absolute errors of $\mathcal{U}$ and $\mathcal{V}$ for $\mathcal{N}=2, \lambda=1$ and $\psi(t)=\sin(t)$, providing further insight into their structural behaviour. Table 7 reports the value of the cost function $\mathcal{J}$ and computational time for $\psi(t)=t, \lambda=3, \zeta=1, \epsilon_1=\epsilon_2=1$ and $\mathcal{N}=2$ with different values of m and $\tilde{m}$.

Example 5.4: Consider the following 3D-ψ-TFOCPs:

$$
\begin{aligned}
\min\ \mathcal{J}[\mathcal{U},\mathcal{V}]
&= \int_0^1\int_0^1\int_0^1 ((e^{-\lambda\psi(t)}(\psi(t)-\psi(0))^2x^2y^2 \\
&\quad - \mathcal{U}(x,y,t))^2 \\
&\quad + (e^{-\lambda\psi(t)}(\psi(t)-\psi(0))\sin(xy) \\
&\quad - \mathcal{V}(x,y,t))^2)\,\mathrm{d}x\,\mathrm{d}y\,\mathrm{d}t, \qquad (62)
\end{aligned}
$$

under the following constraint

$$
\begin{cases}
{}^{TC}\mathcal{D}^{\zeta,\lambda}_{\psi,t}\mathcal{U}(x,y,t)=\mathcal{U}_{xx}(x,y,t)+\mathcal{U}_{yy}(x,y,t) \\
\quad +\mathcal{V}(x,y,t)+\mathcal{F}(x,y,t), \\
\mathcal{U}(x,y,0)=0, \quad 0<x,y\le 1, \\
\mathcal{U}(x,0,t)=0, \quad \mathcal{U}(x,1,t)=e^{-\lambda\psi(t)} \\
\quad \times(\psi(t)-\psi(0))^2x^2, \quad 0<x,t\le 1. \\
\mathcal{U}(0,y,t)=0, \quad \mathcal{U}(1,y,t)=e^{-\lambda\psi(t)} \\
\quad \times(\psi(t)-\psi(0))^2y^2, \quad 0<y,t\le 1.
\end{cases} \qquad (63)
$$

The exact solution corresponding to the aforementioned problem is given by:

$$
\begin{aligned}
&\langle \mathcal{U}(x,y,t),\mathcal{V}(x,y,t),\mathcal{J}\rangle \\
&\quad = \langle e^{-\lambda\psi(t)}(\psi(t)-\psi(0))^2x^2y^2, \\
&\qquad e^{-\lambda\psi(t)}(\psi(t)-\psi(0))\sin(xy),0\rangle.
\end{aligned}
$$

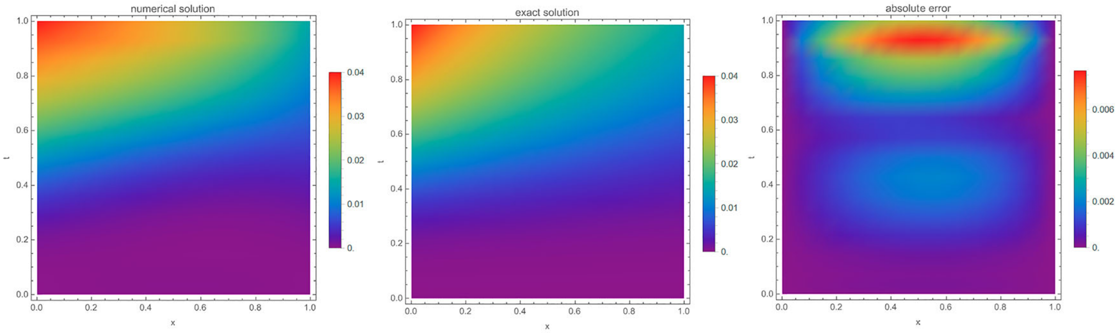

Figure 6. The density distributions of numerical, exact solutions and their absolute errors with $\zeta = 0.75, \mathcal{N} = 2, \lambda = 3$ and $\psi(t) = \sin(t)$ (Example 5.3).

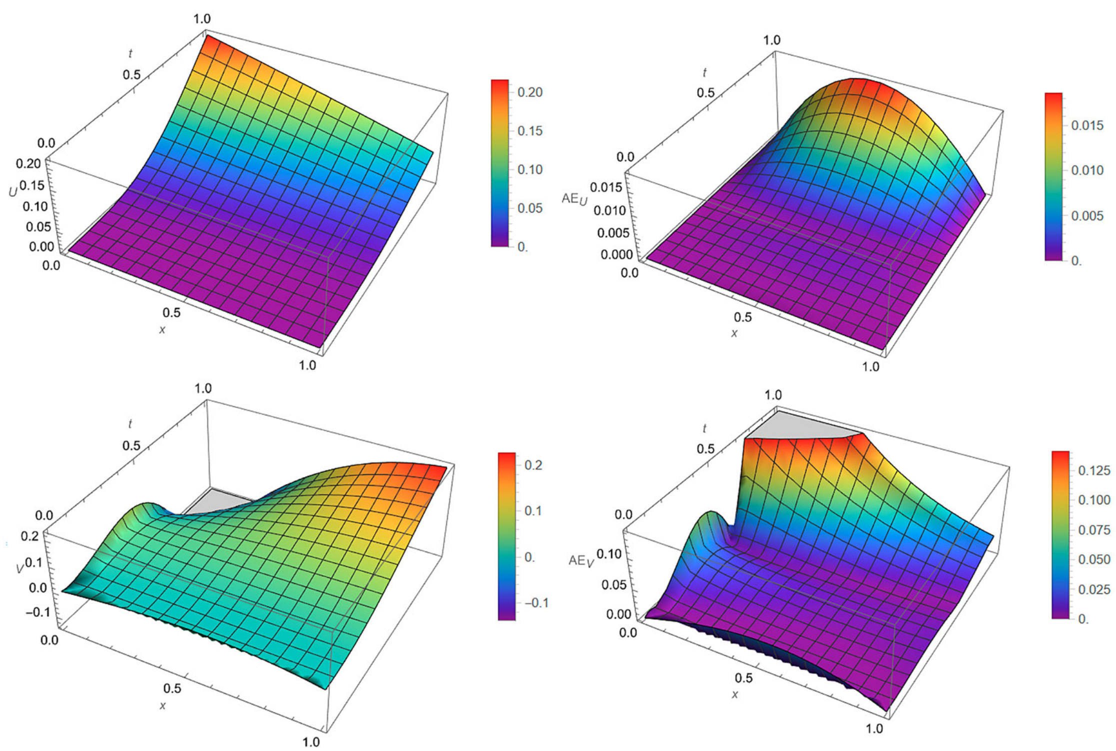

Figure 7. The numerical solutions and their corresponding absolute errors with $\zeta = 0.95, \mathcal{N} = 2, \lambda = 1$ and $\psi(t) = \sin(t)$ (Example 5.3).

Table 5. The $N_{\mathcal{U}}$ and $AE_{\mathcal{U}}$ for $\zeta = 0.95, \mathcal{N} = 2$ and $\psi(t) = t$ (Example 5.3).

	$\lambda = 0$		$\lambda = 1$		$\lambda = 3$		$\lambda = 5$	
(x, t)	$N_{\mathcal{U}}$	$AE_{\mathcal{U}}$	$N_{\mathcal{U}}$	$AE_{\mathcal{U}}$	$N_{\mathcal{U}}$	$AE_{\mathcal{U}}$	$N_{\mathcal{U}}$	$AE_{\mathcal{U}}$
(0.1, 0.1)	0.000094	3.88×10^{-6}	0.000078	4.10×10^{-6}	0.000050	1.69×10^{-5}	0.000033	2.18×10^{-5}
(0.2, 0.2)	0.001062	2.48×10^{-4}	0.000767	3.06×10^{-4}	0.000292	4.26×10^{-4}	−0.000039	5.21×10^{-4}
(0.3, 0.3)	0.005445	5.55×10^{-4}	0.003545	9.00×10^{-4}	0.000671	1.77×10^{-3}	−0.001464	2.80×10^{-3}
(0.4, 0.4)	0.016867	2.94×10^{-4}	0.009964	1.54×10^{-3}	0.000237	4.93×10^{-3}	−0.007939	1.03×10^{-2}
(0.5, 0.5)	0.039186	1.28×10^{-3}	0.021050	1.94×10^{-3}	−0.002785	1.12×10^{-2}	−0.027303	3.04×10^{-2}
(0.6, 0.6)	0.075717	4.59×10^{-3}	0.037083	1.95×10^{-3}	−0.010366	2.21×10^{-2}	−0.073734	7.73×10^{-2}
(0.7, 0.7)	0.128450	9.22×10^{-3}	0.057610	1.60×10^{-3}	−0.023230	3.78×10^{-2}	−0.166847	1.70×10^{-1}
(0.8, 0.8)	0.197291	1.32×10^{-2}	0.081630	1.07×10^{-3}	−0.037606	5.43×10^{-2}	−0.312855	3.16×10^{-1}
(0.9, 0.9)	0.279289	1.25×10^{-2}	0.107903	5.50×10^{-4}	−0.037992	5.59×10^{-2}	−0.419152	4.22×10^{-1}
$\mathcal{J}$	1.71102×10^{-6}		6.55063×10^{-6}		3.28309×10^{-5}		6.88835×10^{-5}	
CPU	6.562		4.515		4.000		3.860	

Table 6. The $AE_{\mathcal{U}}$ and $AE_{\mathcal{V}}$ for $\zeta = 0.95, \mathcal{N} = 3$ and $\lambda = 1$ (Example 5.3).

	$\psi(t) = t$		$\psi(t) = \sinh(t)$		$\psi(t) = \sin(t)$	
(x, t)	$AE_{\mathcal{U}}$	$AE_{\mathcal{V}}$	$AE_{\mathcal{U}}$	$AE_{\mathcal{V}}$	$AE_{\mathcal{U}}$	$AE_{\mathcal{V}}$
(0.1, 0.1)	5.16×10^{-6}	9.55×10^{-4}	6.07×10^{-6}	1.08×10^{-3}	3.84×10^{-6}	8.40×10^{-4}
(0.2, 0.2)	3.09×10^{-4}	8.57×10^{-3}	3.69×10^{-4}	1.06×10^{-2}	2.51×10^{-4}	6.82×10^{-3}
(0.3, 0.3)	9.13×10^{-4}	1.72×10^{-2}	1.33×10^{-3}	2.59×10^{-2}	5.63×10^{-4}	1.06×10^{-2}
(0.4, 0.4)	1.57×10^{-3}	2.66×10^{-2}	3.27×10^{-3}	5.24×10^{-2}	4.11×10^{-4}	9.84×10^{-3}
(0.5, 0.5)	2.02×10^{-3}	3.63×10^{-2}	7.41×10^{-3}	1.02×10^{-1}	6.83×10^{-4}	3.99×10^{-3}
(0.6, 0.6)	2.09×10^{-3}	4.60×10^{-2}	1.70×10^{-2}	2.04×10^{-1}	2.72×10^{-3}	5.83×10^{-3}
(0.7, 0.7)	1.81×10^{-3}	5.53×10^{-2}	3.97×10^{-2}	4.34×10^{-1}	4.97×10^{-3}	1.69×10^{-2}
$\mathcal{J}$	6.80953×10^{-6}		1.47298×10^{-5}		2.73570×10^{-6}	
CPU	8.813		7.156		11.781	

Table 7. The value of the cost function $\mathcal{J}$ and computational time for $\psi(t) = t, \lambda = 3, \zeta = 1$, and $\mathcal{N} = 3$ (Example 5.3).

Method	$m = 1, \tilde{m} = 2$	$m = 2, \tilde{m} = 1$	$m = \tilde{m} = 2$
$\mathcal{J}$	8.79320×10^{-2}	1.12020×10^{-3}	2.03364×10^{-4}
CPU	0.375	0.937	4.047

The approach described in Section 3 is implemented with $m = \tilde{m} = 2$, and $\epsilon_1 = \epsilon_2 = \frac{1}{5}$. Table 8 provides the numerical solutions of $\mathcal{U}$ together with their absolute errors for the case $\zeta = 0.95$, $\mathcal{N} = 2$, and $\psi(t) = t$, evaluated across different values of λ. Table 9 summarises the numerical solutions of $\mathcal{U}$ together with their absolute errors for $\zeta = 0.75$, $\mathcal{N} = 2$, and $\lambda = 3$, obtained under various selections of ψ. In addition, these tables report the values of the cost function and computational time. Figure 8 depicts the density distributions of the numerical and exact solutions, along with their corresponding absolute errors, for $\zeta = 0.75, \mathcal{N} = 2, \lambda = 3$ and $\psi(t) = \sin(t)$ in $x = y = 0.75$. Finally, Figure 9 presents a three-dimensional visualisation of the numerical solutions $\mathcal{U}$ and $\mathcal{V}$ for $\zeta = 0.95, \mathcal{N} = 2, \lambda = 3$ and $\psi(t) = \sin(t)$ in $y = 0.75$, thereby offering deeper insight into their structural characteristics.

6. Conclusion

In conclusion, this work presented a pioneering numerical framework for efficiently solving 2D and 3D-ψ-TFOCPs. By recasting the original problems into equivalent variational forms and employing DNNs with the FBFs and *sinh* as activation functions, the method achieved highly accurate approximations of the state variable using a relatively small number of basis function. The formulation of integral operators and their discretization via the Fejér quadrature rule, specifically tailored to the generalised ψ-tempered fractional calculus, ensured both numerical stability and precision. The transformation of the control problems into nonlinear algebraic systems and their solution via Newton's iterative method demonstrated the practical efficiency of the approach. Distinguished by its simplicity, computational efficiency, and rigorous convergence guarantees, the proposed methodology was validated through four illustrative examples, confirming its applicability to real-world problems. The findings clearly underscore the practical significance of the proposed methodology, demonstrating its ability to enhance both accuracy and computational efficiency while offering strong potential for impactful real-world engineering and scientific applications.

Beyond these case-specific findings, the results also offer broader insights for optimal control theory. The demonstrated ability of the deep fractional-order framework to handle high-dimensional, nonlinear, and memory-dependent systems indicates its generalisability to a wide spectrum of optimal control problems. In particular, the integration of ψ-tempered fractional operators with deep learning architectures provides a flexible modelling paradigm capable of capturing complex temporal dynamics, long-range interactions, and variable memory effects-features that frequently arise in engineering, physics, biology, and economics. Thus, the proposed methodology not only advances numerical strategies for fractional control systems but also contributes conceptually to understanding and solving modern optimal control problems with nonlocal and history-dependent behaviour. In future research, we intend to pursue the following directions:

- Extending the proposed methodology to higher-dimensional nonlinear FOCPs with more complex

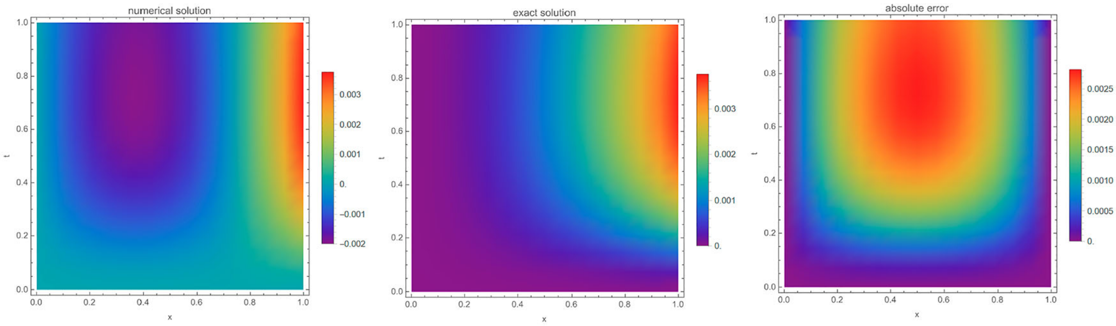

Figure 8. The density distributions of numerical, exact solutions and their absolute errors with $\zeta = 0.75, \mathcal{N} = 2, \lambda = 3$ and $\psi(t) = \sin(t)$ (Example 5.4).

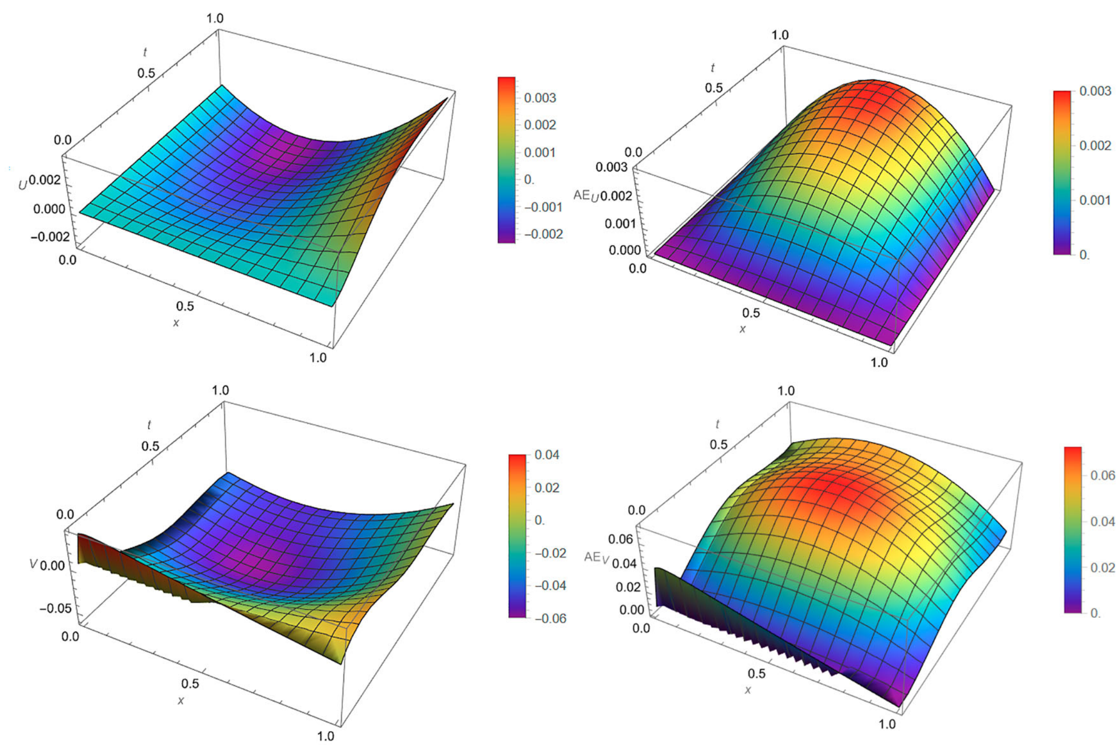

Figure 9. The numerical solutions and their corresponding absolute errors with $\zeta = 0.95, \mathcal{N} = 2, \lambda = 3$ and $\psi(t) = \sin(t)$ (Example 5.4).

Table 8. The $N_{\mathcal{U}}$ and $AE_{\mathcal{U}}$ for $\zeta = 0.95, \mathcal{N} = 2$ and $\psi(t) = t$ (Example 5.4).

	$\lambda = 0$		$\lambda = 1$		$\lambda = 3$		$\lambda = 5$	
(x, y, t)	$N_{\mathcal{U}}$	$AE_{\mathcal{U}}$	$N_{\mathcal{U}}$	$AE_{\mathcal{U}}$	$N_{\mathcal{U}}$	$AE_{\mathcal{U}}$	$N_{\mathcal{U}}$	$AE_{\mathcal{U}}$
(0.1, 0.1, 0.1)	−0.000080	8.10×10^{-5}	−0.000072	7.33×10^{-5}	−0.000059	6.00×10^{-5}	−0.000049	4.92×10^{-5}
(0.2, 0.2, 0.2)	−0.000960	1.02×10^{-3}	−0.000786	8.38×10^{-4}	−0.000527	5.62×10^{-4}	−0.000270	2.94×10^{-4}
(0.3, 0.3, 0.3)	−0.003240	3.97×10^{-3}	−0.002400	2.94×10^{-3}	−0.001317	1.61×10^{-3}	−0.000023	1.85×10^{-4}
(0.4, 0.4, 0.4)	−0.005120	9.22×10^{-3}	−0.003432	6.18×10^{-3}	−0.001542	2.77×10^{-3}	0.002644	2.09×10^{-3}
(0.5, 0.5, 0.5)	0.000000	1.56×10^{-3}	0.000000	9.48×10^{-3}	0.000000	3.49×10^{-3}	0.011695	1.04×10^{-3}
(0.6, 0.6, 0.6)	0.025920	2.07×10^{-2}	0.014225	1.14×10^{-2}	0.004285	3.42×10^{-3}	0.033739	3.14×10^{-2}
(0.7, 0.7, 0.7)	0.096040	2.16×10^{-2}	0.047692	1.07×10^{-2}	0.011761	2.65×10^{-3}	0.074229	7.07×10^{-2}
(0.8, 0.8, 0.8)	0.245760	1.64×10^{-2}	0.110427	7.36×10^{-3}	0.022295	1.49×10^{-3}	0.119323	1.15×10^{-1}
(0.9, 0.9, 0.9)	0.524880	6.56×10^{-3}	0.213400	2.67×10^{-3}	0.035275	4.41×10^{-4}	0.103910	9.80×10^{-2}
$\mathcal{J}$	2.31027×10^{-3}		1.51394×10^{-3}		6.50128×10^{-4}		1.44433×10^{-3}	
CPU	51.204		55.078		49.688		131.297	

Table 9. The $N_{\mathcal{U}}$ and $AE_{\mathcal{U}}$ for $\zeta = 0.75, \mathcal{N} = 2$ and $\lambda = 3$ (Example 5.4).

	$\psi(t) = t$		$\psi(t) = \sinh(t)$		$\psi(t) = \sin(t)$	
(x, y, t)	$N_{\mathcal{U}}$	$AE_{\mathcal{U}}$	$N_{\mathcal{U}}$	$AE_{\mathcal{U}}$	$N_{\mathcal{U}}$	$AE_{\mathcal{U}}$
$(0.1, 0.1, 0.1)$	-0.000059	6.00×10^{-5}	-0.000066	6.72×10^{-5}	-0.000059	3.25×10^{-3}
$(0.2, 0.2, 0.2)$	-0.000527	5.62×10^{-4}	-0.000531	5.66×10^{-4}	-0.000522	5.57×10^{-4}
$(0.3, 0.3, 0.3)$	-0.001317	1.61×10^{-3}	-0.001195	1.50×10^{-3}	-0.001296	1.59×10^{-3}
$(0.4, 0.4, 0.4)$	-0.001542	2.78×10^{-3}	-0.000718	1.98×10^{-3}	-0.001509	2.72×10^{-3}
$(0.5, 0.5, 0.5)$	0.000000	3.49×10^{-3}	0.003969	4.15×10^{-4}	0.000000	3.41×10^{-3}
$(0.6, 0.6, 0.6)$	0.004285	3.43×10^{-3}	0.022450	1.47×10^{-2}	0.004219	3.38×10^{-3}
$(0.7, 0.7, 0.7)$	0.011761	2.65×10^{-3}	0.101124	8.69×10^{-2}	0.011776	2.65×10^{-3}
$(0.8, 0.8, 0.8)$	0.022295	1.49×10^{-3}	0.507211	4.85×10^{-1}	0.022970	1.53×10^{-3}
$(0.9, 0.9, 0.9)$	0.035275	4.41×10^{-4}	2.392590	2.36×10^{0}	0.037921	3.72×10^{-3}
$\mathcal{J}$	5.39495×10^{-4}		7.23881×10^{-4}		5.29732×10^{-4}	
CPU	78.531		170.094		89.484	

boundary conditions, as well as to multi-objective and stochastic fFOCPs.

- Applying the framework to other classes of optimal control problems, including adaptive and multi-objective settings.
- Implementing the methodology on experimental datasets or in real-time applications to further assess its practical validity and robustness.
- Investigating the method for more challenging scenarios, including non-smooth solutions, stiff regimes, strong memory effects, delayed responses, and noisy data, to demonstrate its applicability in realistic and complex ψ-tempered fractional control systems.
- Extending the framework to error estimation in other norms, such as L^2, L^∞, or weighted fractional norms, to provide a more comprehensive assessment of approximation accuracy.
- Combining the proposed methodology with other deep optimisation techniques, such as reinforcement learning, to handle dynamic or time-dependent fractional optimal control problems and further enhance adaptability in complex environments.

Acknowledgments

We express our sincere thanks to the anonymous referees for their valuable suggestions that improved the final manuscript. All authors contributed equally and significantly in writing this article. All authors read and approved the final manuscript.

Data availability statement

Data will be made available on reasonable request.

Disclosure statement

No potential conflict of interest was reported by the author(s).

References

Alizadeh, A., & Effati, S. (2018). An iterative approach for solving fractional optimal control problems. *Journal of Vibration and Control*, *24*(1), 18–36. https://doi.org/10.1177/1077546316633391

Baeumer, B., & Meerschaert, M. M. (2010). Tempered stable Lévy motion and transient super-diffusion. *Journal of Computational and Applied Mathematics*, *233*(10), 2438–2448. https://doi.org/10.1016/j.cam.2009.10.027

Baitiche, Z., Derbazi, C., Alzabut, J., Samei, M. E., Kaabar, M. K., & Siri, Z. (2021). Monotone iterative method for ψ-Caputo fractional differential equation with nonlinear boundary conditions. *Fractal and Fractional*, *5*(3), 81. https://doi.org/10.3390/fractalfract5030081

Canuto, C., Hussaini, M. Y., Quarteroni, A., & Zang, T. A. (2006). *Spectral methods: fundamentals in single domains*. Springer.

Carpinteri, A., & Mainardi, F. (2014). *Fractals and fractional calculus in continuum mechanics*. Springer.

Chakraborty, A., & Veeresha, P. (2024). Effects of global warming, time delay and chaos control on the dynamics of a chaotic atmospheric propagation model within the frame of Caputo fractional operator. *Communications in Nonlinear Science and Numerical Simulation*, *128*,107657. https://doi.org/10.1016/j.cnsns.2023.107657

Dufera, T. T. (2021). Deep neural network for system of ordinary differential equations: Vectorized algorithm and simulation. *Machine Learning with Applications*, *5*,100058. https://doi.org/10.1016/j.mlwa.2021.100058

Fahad, H. M., Fernandez, A., Rehman, M. U., & Siddiqi, M. (2021). Tempered and Hadamard-type fractional calculus with respect to functions. *Mediterranean Journal of Mathematics*, *18*(4), 143. https://doi.org/10.1007/s00009-021-01783-9

Fernandez, A., & Fahad, H. M. (2022). Weighted fractional calculus: A general class of operators. *Fractal and Fractional*, *6*(4), 208. https://doi.org/10.3390/fractalfract6040208

Guo, H., Zhuang, X., & Rabczuk, T. (2021). A deep collocation method for the bending analysis of Kirchhoff plate. Preprint arXiv:2102.02617.

Hajimohammadi, Z., Parand, K., & Ghodsi, A. (2021). Legendre deep neural network (LDNN) and its application for approximation of nonlinear Volterra Fredholm Hammerstein integral equations. Preprint. arXiv:2106.14320.

Heydari, M. H., & Razzaghi, M. (2022). A new class of orthonormal basis functions: Application for fractional optimal control problems. *International Journal of Systems Science*, *53*(2), 240–252. https://doi.org/10.1080/00207721.2021.1947411

Heydari, M. H., & Razzaghi, M. (2024). A new wavelet method for fractional integro-differential equations with ψ-Caputo fractional derivative. *Mathematics and Computers in Simulation*, *217*, 97–108. https://doi.org/10.1016/j.matcom.2023.10.023

Heydari, M. H., Razzaghi, M., & Cattani, C. (2023). Fractional Chebyshev cardinal wavelets: Application for fractional quadratic integro-differential equations. *International Journal of Computer Mathematics*, *100*(3), 479–496. https://doi.org/10.1080/00207160.2022.2122052

Hinton, G. E., Osindero, S., & Teh, Y. W. (2006). A fast learning algorithm for deep belief nets. *Neural Computation*, *18*(7), 1527–1554. https://doi.org/10.1162/neco.2006.18.7.1527

Javad Ebadi, M. (2025). A novel approach to nonlinear 2D fractional optimal control problems via generalized lerch polynomials. *Mathematical Methods in the Applied Sciences*, *48*(13), 12738–12748. https://doi.org/10.1002/mma.v48.13

Kumar, N., & Mehra, M. (2021). Legendre wavelet collocation method for fractional optimal control problems with fractional Bolza cost. *Numerical Methods for Partial Differential Equations*, *37*(2), 1693–1724. https://doi.org/10.1002/num.v37.2

Li, C., Deng, W., & Zhao, L. (2015). Well-posedness and numerical algorithm for the tempered fractional ordinary differential equations. Preprint. arXiv:1501.00376.

Li, C., N'Gbo, N. G., & Su, F. (2024). Finite difference methods for nonlinear fractional differential equation with ψ-Caputo derivative. *Physica D: Nonlinear Phenomena*, *460*,134103. https://doi.org/10.1016/j.physd.2024.134103

Mali, A. D., Kucche, K. D., Fernandez, A., & Fahad, H. M. (2022). On tempered fractional calculus with respect to functions and the associated fractional differential equations. *Mathematical Methods in the Applied Sciences*, *45*(17), 11134–11157. https://doi.org/10.1002/mma.v45.17

Mashayekhi, S., Ordokhani, Y., & Razzaghi, M. (2013). Hybrid functions approach for optimal control of systems described by integro-differential equations. *Applied Mathematical Modelling*, *37*(5), 3355–3368. https://doi.org/10.1016/j.apm.2012.07.014

Mashayekhi, S., Razzaghi, M., & Wattanataweekul, M. (2016). Analysis of multi-delay and piecewise constant delay systems by hybrid functions approximation. *Differential Equations and Dynamical Systems*, *24*(1), 1–20. https://doi.org/10.1007/s12591-014-0203-0

Meerschaert, M. M., Sabzikar, F., Phanikumar, M. S., & Zeleke, A. (2014). Tempered fractional time series model for turbulence in geophysical flows. *Journal of Statistical Mechanics: Theory and Experiment*, *2014*(9), P09023. https://doi.org/10.1088/1742-5468/2014/09/P09023

Morgado, M. L., & Rebelo, M. (2017). Well-posedness and numerical approximation of tempered fractional terminal value problems. *Fractional Calculus and Applied Analysis*, *20*(5), 1239–1262. https://doi.org/10.1515/fca-2017-0065

Nassif, A. B., Shahin, I., Attili, I., Azzeh, M., & Shaalan, K. (2019). Speech recognition using deep neural networks: A systematic review. *IEEE Access*, *7*, 19143–19165. https://doi.org/10.1109/ACCESS.2019.2896880

Oumarou, C. M., Fahad, H. M., Djida, J. D., & Fernandez, A. (2021). On fractional calculus with analytic kernels with respect to functions. *Computational and Applied Mathematics*, *40*(7), 244. https://doi.org/10.1007/s40314-021-01622-3

Qing, W., & Pan, B. (2024). Modified fractional homotopy method for solving nonlinear optimal control problems. *Nonlinear Dynamics*, *112*(5), 3453–3479. https://doi.org/10.1007/s11071-023-09191-2

Qiu, W., Nikan, O., & Avazzadeh, Z. (2023). Numerical investigation of generalized tempered-type integrodifferential equations with respect to another function. *Fractional Calculus and Applied Analysis*, *26*(6), 2580–2601. https://doi.org/10.1007/s13540-023-00198-5

Rabiei, K., & Parand, K. (2020). Collocation method to solve inequality-constrained optimal control problems of arbitrary order. *Engineering with Computers*, *36*(1), 115–125. https://doi.org/10.1007/s00366-018-0688-1

Rahimkhani, P. (2023). Numerical solution of nonlinear stochastic differential equations with fractional Brownian motion using fractional-order Genocchi deep neural networks. *Communications in Nonlinear Science and Numerical Simulation*, *126*,107466. https://doi.org/10.1016/j.cnsns.2023.107466

Rahimkhani, P., & Abdeljawad, T. (2025). Application of χ-fractional Genocchi wavelets for solving χ-fractional differential equations. *Mathematics and Computers in Simulation*, *239*, 790–804. https://doi.org/10.1016/j.matcom.2025.07.031

Rahimkhani, P., & Heydari, M. H. (2023). Fractional shifted Morgan-Voyce neural networks for solving fractal-fractional pantograph differential equations. *Chaos, Solitons & Fractals*, *175*,114070. https://doi.org/10.1016/j.chaos.2023.114070

Rahimkhani, P., & Ordokhani, Y. (2021). Numerical investigation of distributed-order fractional optimal control problems via Bernstein wavelets. *Optimal Control Applications and Methods*, *42*(1), 355–373. https://doi.org/10.1002/oca.v42.1

Rahimkhani, P., Ordokhani, Y., & Babolian, E. (2016). Fractional-order Bernoulli wavelets and their applications. *Applied Mathematical Modelling*, *40*(17-18), 8087–8107. https://doi.org/10.1016/j.apm.2016.04.026

Rahimkhani, P., Ordokhani, Y., & Sedaghat, S. (2023). The numerical treatment of fractal-fractional 2D optimal control problems by Müntz-Legendre polynomials. *Optimal Control Applications and Methods*, *44*(6), 3033–3051. https://doi.org/10.1002/oca.v44.6

Rahimkhani, P., Sabermahani, S., & Hassani, H. (2025). Physics informed neural network method for solving delay Hilfer fractional differential equations. *International*

Journal of Numerical Modelling: Electronic Networks, Devices and Fields, *38*(3), e70070. https://doi.org/10.1002/jnm.v38.3

Sahu, P. K., & Saha Ray, S. (2018). Comparison on wavelets techniques for solving fractional optimal control problems. *Journal of Vibration and Control*, *24*(6), 1185–1201. https://doi.org/10.1177/1077546316659611

Santra, S., & Mohapatra, J. (2022). Analysis of a finite difference method based on L1 discretization for solving multi-term fractional differential equation involving weak singularity. *Mathematical Methods in the Applied Sciences*, *45*(11), 6677–6690. https://doi.org/10.1002/mma.v45.11

Sayevand, K., Zarvan, Z., & Nikan, O. (2022). On approximate solution of optimal control problems by parabolic equations. *International Journal of Applied and Computational Mathematics*, *8*(5), 248. https://doi.org/10.1007/s40819-022-01454-7

Vaziri, A., & Fang, H. (2025). Optimal inferential control of convolutional neural networks. In *2025 American Control Conference (ACC)* (pp. 2603–2610). IEEE.

Xu, X., Xiong, L., & Zhou, F. (2021). Solving fractional optimal control problems with inequality constraints by a new kind of Chebyshev wavelets method. *Journal of Computational Science*, *54*,101412. https://doi.org/10.1016/j.jocs.2021.101412

Yang, L., MacEachren, A. M., Mitra, P., & Onorati, T. (2018). Visually-enabled active deep learning for (geo) text and image classification: A review. *ISPRS International Journal of Geo-Information*, *7*(2), 65. https://doi.org/10.3390/ijgi7020065

Youssri, Y. H., & Atta, A. G. (2024). Fejér-quadrature collocation algorithm for solving fractional integro-differential equations via Fibonacci polynomials. *Contemporary Mathematics*, *5*, 296–308. https://doi.org/10.37256/cm.512024

Zaky, M. A. (2019). Existence, uniqueness and numerical analysis of solutions of tempered fractional boundary value problems. *Applied Numerical Mathematics*, *145*, 429–457. https://doi.org/10.1016/j.apnum.2019.05.008

Zeid, S. S., & Yousefi, M. (2016). Approximated solutions of linear quadratic fractional optimal control problems. *Journal of Applied Mathematics, Statistics and Informatics*, *12*(2), 83–94. https://doi.org/10.1515/jamsi-2016-0010

Zhao, L., Deng, W., & Hesthaven, J. S. (2016). Spectral methods for tempered fractional differential equations. Preprint. arXiv:1603.06511.

Zurigat, M., Momani, S., Odibat, Z., & Alawneh, A. (2010). The homotopy analysis method for handling systems of fractional differential equations. *Applied Mathematical Modelling*, *34*(1), 24–35. https://doi.org/10.1016/j.apm.2009.03.024